

# Data-Driven Structural Health Monitoring of Short Carbon Fiber-Reinforced Polymer Composites via Multiphysics Phase-Field Simulation

Behrouz Arash<sup>a,b,\*</sup>, Shadab Zakavati<sup>a</sup>, Quan Wang<sup>c</sup>, Timon Rabczuk<sup>d</sup>

<sup>a</sup>*Department of Mechanical, Electrical and Chemical Engineering, Oslo Metropolitan University, Pilestredet 35, 0166 Oslo, Norway*

<sup>b</sup>*Green Energy Lab, Department of Mechanical, Electrical and Chemical Engineering, OsloMet - Oslo Metropolitan University, Oslo, Norway*

<sup>c</sup>*College of Engineering, Shantou University, Shantou, Guangdong 515063, China*

<sup>d</sup>*Institute of Structural Mechanics, Bauhaus-Universität Weimar, Marienstraße 15, 99423 Weimar, Germany*

---

## Abstract

Short carbon fiber-reinforced polymer (SCFRP) composites exploit the intrinsic conductivity of the carbon fiber network for self-sensing, yet no predictive model couples their anisotropic, rate-dependent fracture to piezoresistive damage identification. This work presents a finite-deformation multiphysics phase-field framework coupling a viscoelastic-viscoplastic constitutive model, an anisotropic crack resistance formulation, and a piezoresistive conductivity model. The three sub-problems are unified through the second-order fiber orientation tensor, which simultaneously defines fiber family directions, crack resistance anisotropy, and principal conduction paths of the carbon fiber network. A damage-coupled conductivity tensor captures both strain-driven geometric-kinematic resistance changes and irreversible network severance driven by the phase-field variable. The framework is coupled to an eight-electrode electrical impedance tomography configuration, and the normalized inter-electrode conductance ratios serve as inputs to a feedforward artificial neural network that infers normalized crack length and mechanical compliance without mechanical sensing. The network achieves  $R^2 = 0.99$  on held-out configurations, confirming generalization across the microstructure space. The framework establishes a physics-based, computationally efficient route for real-time structural health monitoring and inverse damage assessment in SCFRP composites.

*Keywords:* Short carbon fiber/epoxy composites, Piezoresistive self-sensing, Phase-field fracture, Structural health monitoring, Artificial neural network

---

\*Corresponding author

*Email addresses:* behrouza@oslomet.no (Behrouz Arash), wangquan@stu.edu.cn (Quan Wang), timon.rabczuk@uni-weimar.de (Timon Rabczuk)

## 1. Introduction

Short carbon fiber-reinforced polymer (SCFRP) composites have become indispensable in aerospace, automotive, and renewable energy applications owing to their high specific stiffness and strength, tailorable anisotropy, and the intrinsic electrical conductivity of the carbon fiber (CF) network [1–3]. This electrical conductivity gives SCFRP composites a dual functionality: they serve simultaneously as load-bearing structural members and as self-sensing elements capable of detecting internal damage through changes in their electrical resistance [4, 5]. Realizing this self-sensing potential in service, however, requires predictive models that couple the anisotropic, rate-dependent mechanical behavior and fracture of the composite to its evolving electrical response, a coupling that remains largely absent from the literature.

The mechanical response of SCFRP composites exhibits pronounced anisotropy governed by fiber orientation distributions, which controls not only elastic properties but also inelastic deformation mechanisms and fracture behavior [3, 6, 7]. Polymer matrices additionally exhibit rate-dependent behavior through coupled viscoelastic and viscoplastic mechanisms [8–10], and hygrothermal conditions further degrade material performance through moisture absorption and thermal cycling [10–12]. The interplay between mechanical anisotropy, rate-dependent inelasticity, environmental degradation, and damage evolution presents formidable challenges for predictive modeling frameworks.

Phase-field modeling has emerged as a variational framework for fracture that overcomes the limitations of cohesive zone models [13, 14], element deletion techniques [15], and extended finite element methods [16, 17] by representing cracks through a continuous damage field, eliminating explicit crack tracking and providing mesh-independent solutions [18–22]. The framework has been extended to brittle [23, 24], ductile [25–27], cohesive fracture [28], anisotropic fracture energy [29–31], dynamic effects [32], and multi-field coupling [10, 33, 34].

Anisotropic phase-field models for fiber-reinforced composites introduce directionally dependent fracture energy that reflects preferential crack paths imposed by fiber orientation [35–38]. Structural tensor-based formulations capture orientation-dependent fracture resistance [29, 30], and multi-phase-field frameworks resolve simultaneously intralaminar cracking and interlaminar delamination in laminated composites [27, 37, 39]. Phase-field models incorporating hydro-mechanical coupling have also emerged [10, 40], though most existing anisotropic formulations consider elastic or small-strain elasto-plastic behavior [41, 42], with limited attention to the coupled viscoelastic-viscoplastic response of polymer matrices at finite deforma-

tion [43, 44]. For polymer-based materials, phase-field frameworks incorporating viscoelastic behavior have been developed [45–48], and Arash and coworkers [9, 49, 50] extended these to finite-deformation viscoelastic-viscoplastic fracture with hygrothermal coupling for short fiber-reinforced polymer composites. The combination of viscoelastic and viscoplastic mechanisms within phase-field fracture frameworks has not, however, been coupled to the electrical self-sensing response of the carbon fiber network, and no existing framework integrates this mechanical-fracture model with inverse damage identification for structural health monitoring.

The piezoresistive self-sensing capability of SCFRPs has been studied experimentally for several decades [4, 5, 51]. Two physically distinct mechanisms contribute to resistance changes under mechanical loading: a geometric-kinematic mechanism, in which deformation alters effective conduction path lengths and fiber contact geometry; and a damage-driven mechanism, in which matrix cracking and fiber-matrix debonding irreversibly sever conductive pathways [51, 52]. Despite this rich experimental foundation, predictive computational models coupling these mechanisms to a continuum fracture framework remain scarce. Existing electrical models typically assume linear piezoresistivity with prescribed damage [53] and do not account for the anisotropic, orientation-dependent conductivity tensor or its evolution with the phase-field damage variable. Furthermore, no study has combined piezoresistive phase-field simulation with a multi-electrode measurement setup and machine learning inversion for real-time structural health monitoring of SCFRP composites.

Motivated by these considerations, the present work develops an integrated multiphysics phase-field framework for modeling anisotropic viscoelastic-viscoplastic fracture and damage-induced piezoresistive response in SCFRP composites at finite deformation, and combines it with a data-driven inverse framework for structural health monitoring. The principal contributions are as follows. First, a finite-deformation viscoelastic-viscoplastic constitutive model is formulated through multiplicative decomposition of the deformation gradient, extending the framework of Arash et al. [9, 49, 50] to incorporate piezoresistive self-sensing in anisotropic short fiber composites. Second, an anisotropic phase-field fracture formulation employing the second-order fiber orientation tensor captures orientation-dependent fracture energy for arbitrary fiber architectures. Third, a damage-coupled piezoresistive conductivity tensor captures both geometric-kinematic resistance changes through axial and transverse gauge factors and irreversible damage-driven degradation consistent with the phase-field model. The fiber orientation tensor serves as the common thread: it simultaneously defines fiber family directions, anisotropic crack resistance, and principal conduction paths of the carbon fiber network.

Fourth, the framework is combined with an eight-electrode electrical impedance tomography (EIT) setup and a feedforward artificial neural network (ANN) for real-time inverse damage identification from conductance measurements alone.

The remainder of this paper is organized as follows. Section 2 presents the viscoelastic-viscoplastic constitutive model, detailing the kinematics, stress decomposition, and fiber family representation. Section 3 introduces the anisotropic phase-field fracture formulation. Section 4 develops the piezoresistive model and electric field formulation. Section 5 presents the EIT configuration and the ANN-based inverse framework for structural health monitoring (SHM). Section 6 presents numerical investigations examining the effects of fiber architecture, orientation, content, and temperature on the coupled electromechanical fracture response and SHM performance. Section 7 summarizes the key findings and outlines future research directions.

## 2. Constitutive model for short carbon fiber-reinforced epoxy composites

A finite-deformation viscoelastic-viscoplastic constitutive model is developed for short carbon fiber-reinforced polymer (SCFRP) composites. The model combines the rate-dependent inelastic response of the epoxy matrix with the anisotropic stiffening contributed by multiple carbon fiber families. A schematic of the rheological model and the representative volume element are shown in Fig. 1. The deformation gradient  $\mathbf{F}$ , the viscous internal variable  $\bar{\mathbf{F}}^v$ , and the viscoplastic internal variable  $\bar{\mathbf{F}}^{vp}$  collectively define the state of the material at each material point. As detailed below, the orientation of the carbon fiber families is encoded in a second-order orientation tensor, which serves simultaneously as input to the mechanical constitutive law and to the piezoresistive conductivity model introduced in Section 4.

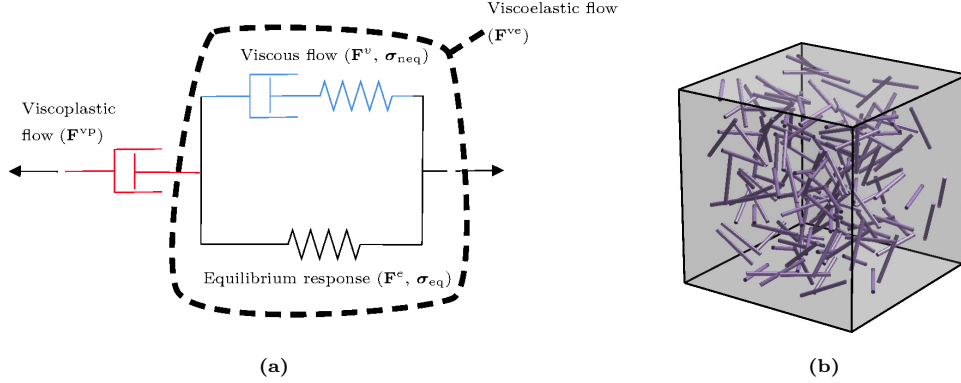


**Figure 1:** (a) One-dimensional schematic of the viscoelastic-viscoplastic constitutive model for SCFRP composites. (b) Representative volume element showing the carbon fiber network embedded in the epoxy matrix.

### 2.1. Kinematics

The total deformation gradient  $\mathbf{F}$  is multiplicatively split into volumetric and isochoric (deviatoric) parts as

$$\mathbf{F} = J^{1/3} \bar{\mathbf{F}}, \quad (1)$$

where  $J = \det[\mathbf{F}]$  is the volumetric Jacobian and  $\bar{\mathbf{F}}$  is the distortional deformation gradient satisfying  $\det[\bar{\mathbf{F}}] = 1$ . The Jacobian is additively split to account for mechanical compressibility and thermal dilatation as

$$J = J_m J_\theta, \quad (2)$$

where  $J_m$  is the purely mechanical volumetric change and

$$J_\theta = 1 + \alpha_\theta (\theta - \theta_0) \quad (3)$$

captures isotropic thermal expansion, with  $\alpha_\theta$  the thermal expansion coefficient,  $\theta$  the absolute temperature, and  $\theta_0 = 296$  K the reference temperature. In the present study, uniform ambient temperature is assumed throughout the specimen, so  $J_\theta$  enters the formulation as a fixed scalar at the start of each simulation.

The distortional deformation gradient is further decomposed multiplicatively into viscoelastic and viscoplastic contributions following the framework of [54]:

$$\bar{\mathbf{F}} = \bar{\mathbf{F}}^{ve} \bar{\mathbf{F}}^{vp}, \quad (4)$$

where  $\bar{\mathbf{F}}^{ve}$  and  $\bar{\mathbf{F}}^{vp}$  denote the viscoelastic and viscoplastic parts of the distortional deformation gradient, respectively. The viscoelastic component is itself split into elastic and viscous

parts:

$$\bar{\mathbf{F}}^{\text{ve}} = \bar{\mathbf{F}}^e \bar{\mathbf{F}}^v. \quad (5)$$

The left Cauchy–Green deformation tensors associated with each intermediate configuration are

$$\bar{\mathbf{B}} = \bar{\mathbf{F}} \bar{\mathbf{F}}^T, \quad (6)$$

$$\bar{\mathbf{B}}^e = \bar{\mathbf{F}}^e (\bar{\mathbf{F}}^e)^T, \quad (7)$$

$$\bar{\mathbf{B}}^{\text{ve}} = \bar{\mathbf{F}}^{\text{ve}} (\bar{\mathbf{F}}^{\text{ve}})^T. \quad (8)$$

The velocity gradient of the viscoelastic network,  $\bar{\mathbf{L}}^{\text{ve}} = \dot{\bar{\mathbf{F}}^{\text{ve}}} (\bar{\mathbf{F}}^{\text{ve}})^{-1}$ , is decomposed into elastic and viscous contributions pushed forward to the current configuration:

$$\bar{\mathbf{L}}^{\text{ve}} = \bar{\mathbf{L}}^e + \bar{\mathbf{F}}^e \bar{\mathbf{L}}^v (\bar{\mathbf{F}}^e)^{-1} = \bar{\mathbf{L}}^e + \tilde{\mathbf{L}}^v, \quad (9)$$

where the viscous velocity gradient in the intermediate configuration is

$$\tilde{\mathbf{L}}^v = \dot{\bar{\mathbf{F}}^v} (\bar{\mathbf{F}}^v)^{-1} = \tilde{\mathbf{D}}^v + \tilde{\mathbf{W}}^v. \quad (10)$$

Here a tilde denotes quantities referred to the intermediate configuration,  $\tilde{\mathbf{D}}^v$  is the symmetric viscous stretching tensor, and  $\tilde{\mathbf{W}}^v$  is the skew-symmetric viscous spin tensor. Following the standard convention [55], the intermediate configuration is rendered unique by setting  $\tilde{\mathbf{W}}^v = \mathbf{0}$ .

The viscous stretching tensor is governed by the Argon flow rule [56]:

$$\tilde{\mathbf{D}}^v = \frac{\dot{\varepsilon}^v}{\tau_{\text{neq}}} \text{dev}[\boldsymbol{\sigma}'_{\text{neq}}], \quad (11)$$

where  $\tau_{\text{neq}} = \|\text{dev}[\boldsymbol{\sigma}_{\text{neq}}]\|_F$  is the Frobenius norm of the non-equilibrium stress deviator,  $\dot{\varepsilon}^v$  is the scalar viscous strain rate, and  $\boldsymbol{\sigma}'_{\text{neq}} = \mathbf{R}_e^T \boldsymbol{\sigma}_{\text{neq}} \mathbf{R}_e$  is the non-equilibrium Cauchy stress rotated to the stress-free intermediate configuration via the elastic rotation  $\mathbf{R}_e$  from the polar decomposition  $\bar{\mathbf{F}}^e = \mathbf{R}_e \mathbf{U}_e$ . The viscous strain rate takes the Arrhenius-type Argon form [57]:

$$\dot{\varepsilon}^v = \dot{\varepsilon}_0 \exp\left[\frac{\Delta H}{k_b T} \left(\left(\frac{\tau_{\text{neq}}}{\tau_0}\right)^m - 1\right)\right], \quad (12)$$

where  $k_b$  is the Boltzmann constant,  $\dot{\varepsilon}_0$  is the pre-exponential strain rate,  $\Delta H$  is the activation energy for viscous flow,  $\tau_0$  is the athermal shear resistance, and  $m$  is a material exponent [12]. From Eqs. (10) and (11), the evolution equation for the viscous deformation gradient follows as

$$\dot{\bar{\mathbf{F}}^v} = (\bar{\mathbf{F}}^e)^{-1} \frac{\dot{\varepsilon}^v}{\tau_{\text{neq}}} \text{dev}[\boldsymbol{\sigma}'_{\text{neq}}] \bar{\mathbf{F}}^{\text{ve}}. \quad (13)$$

The velocity gradient of the total network,  $\bar{\mathbf{L}} = \dot{\bar{\mathbf{F}}}(\bar{\mathbf{F}})^{-1}$ , is likewise split into viscoelastic and viscoplastic parts:

$$\bar{\mathbf{L}} = \bar{\mathbf{L}}^{\text{ve}} + \bar{\mathbf{F}}^{\text{ve}} \bar{\mathbf{L}}^{\text{vp}} (\bar{\mathbf{F}}^{\text{ve}})^{-1} = \bar{\mathbf{L}}^{\text{ve}} + \tilde{\mathbf{L}}^{\text{vp}}. \quad (14)$$

The viscoplastic velocity gradient is decomposed as

$$\tilde{\mathbf{L}}^{\text{vp}} = \dot{\bar{\mathbf{F}}^{\text{vp}}} (\bar{\mathbf{F}}^{\text{vp}})^{-1} = \tilde{\mathbf{D}}^{\text{vp}} + \tilde{\mathbf{W}}^{\text{vp}}, \quad (15)$$

with  $\tilde{\mathbf{W}}^{\text{vp}} = \mathbf{0}$  imposed for uniqueness. The viscoplastic stretching tensor is driven by the total deviatoric Cauchy stress:

$$\tilde{\mathbf{D}}^{\text{vp}} = \frac{\dot{\varepsilon}^{\text{vp}}}{\tau_{\text{tot}}} \text{dev}[\boldsymbol{\sigma}], \quad \tau_{\text{tot}} = \|\text{dev}[\boldsymbol{\sigma}]\|_F. \quad (16)$$

The viscoplastic strain rate is described by a threshold-based phenomenological model:

$$\dot{\varepsilon}^{\text{vp}} = \begin{cases} 0 & \text{if } \tau_{\text{tot}} < \sigma_0, \\ a(\varepsilon - \varepsilon_0)^b \dot{\varepsilon} & \text{if } \tau_{\text{tot}} \geq \sigma_0, \end{cases} \quad (17)$$

where  $a$ ,  $b$ , and  $\sigma_0$  are material constants,  $\varepsilon_0$  marks the onset of viscoplastic flow,  $\varepsilon = \|\mathbf{E}\|_F$  is the Frobenius norm of the Green–Lagrange strain tensor

$$\mathbf{E} = \frac{1}{2}(\mathbf{F}^T \mathbf{F} - \mathbf{I}), \quad (18)$$

and  $\dot{\varepsilon}$  is the scalar strain rate. The corresponding evolution of the viscoplastic deformation gradient is

$$\dot{\bar{\mathbf{F}}^{\text{vp}}} = (\bar{\mathbf{F}}^{\text{ve}})^{-1} \frac{\dot{\varepsilon}^{\text{vp}}}{\tau_{\text{tot}}} \text{dev}[\boldsymbol{\sigma}] \bar{\mathbf{F}}. \quad (19)$$

## 2.2. Implicit time integration

The evolution Eqs. (13) and (19) are first-order nonlinear ODEs whose right-hand sides depend implicitly on the Cauchy stress at the current time  $t_{n+1}$ , which is itself a function of the unknown internal variables. Two numerical difficulties arise. First, a naive explicit update of the form  $\bar{\mathbf{F}}_{n+1}^v = \bar{\mathbf{F}}_n^v + \Delta t \dot{\bar{\mathbf{F}}^v}$  does not preserve the isochoric constraints  $\det(\bar{\mathbf{F}}^v) = \det(\bar{\mathbf{F}}^{\text{vp}}) = 1$ . Second, the implicit coupling between the flow directions and the stress requires an iterative solution within each time step.

Both issues are resolved by an exponential map integrator [58]. For either internal gradient  $\bar{\mathbf{F}}^v$  or  $\bar{\mathbf{F}}^{\text{vp}}$ , the update at time  $t_{n+1}$  reads

$$\bar{\mathbf{F}}_{n+1} = \exp(\Delta t \bar{\mathbf{L}}_{n+1}) \bar{\mathbf{F}}_n. \quad (20)$$

Since the flow rules enforce  $\text{tr}(\bar{\mathbf{L}}^v) = \text{tr}(\bar{\mathbf{L}}^{\text{VP}}) = 0$ , the identity  $\det(\exp(\Delta t \bar{\mathbf{L}})) = \exp(\Delta t \text{tr} \bar{\mathbf{L}}) = 1$  guarantees exact preservation of the isochoric constraint at every iteration. Because  $\bar{\mathbf{L}}_{n+1}$  depends on the unknown stress at  $t_{n+1}$ , the update is solved by fixed-point iteration as summarized in Algorithm 1. The elastic rotation  $\mathbf{R}_e$  required by the algorithm is obtained from the polar decomposition

$$\bar{\mathbf{F}}^e = \mathbf{R}_e \mathbf{U}_e, \quad (21)$$

where  $\mathbf{R}_e$  is proper orthogonal and  $\mathbf{U}_e$  is symmetric positive definite.

---

**Algorithm 1** Implicit time integration over  $[t_n, t_{n+1}]$  with fixed-point iteration.

---

- 1: **Given:**  $\mathbf{F}_{n+1}$ ,  $\bar{\mathbf{F}}_n^v$ ,  $\bar{\mathbf{F}}_n^{\text{VP}}$ ,  $\mathcal{H}_n$ , time step  $\Delta t$ .
  - 2: **Initialize:**  $\bar{\mathbf{F}}^v = \bar{\mathbf{F}}_n^v$ ,  $\bar{\mathbf{F}}^{\text{VP}} = \bar{\mathbf{F}}_n^{\text{VP}}$ , tolerance  $\varepsilon_{\text{tol}}$ , **converged** = false.
  - 3: **while** **converged** = false **do**
  - 4:   **Kinematics:**  $J = \det(\mathbf{F}_{n+1})$ ,  $\bar{\mathbf{F}} = J^{-1/3} \mathbf{F}_{n+1}$ ,  $\bar{\mathbf{F}}^{\text{ve}} = \bar{\mathbf{F}} (\bar{\mathbf{F}}^{\text{VP}})^{-1}$ ,  $\bar{\mathbf{F}}^e = \bar{\mathbf{F}}^{\text{ve}} (\bar{\mathbf{F}}^v)^{-1}$ .
  - 5:   **Stress:** Compute Cauchy stress  $\boldsymbol{\sigma}$  via the constitutive equations of Section 2.3.
  - 6:   **Polar decomposition:**  $\bar{\mathbf{F}}^e = \mathbf{R}_e \mathbf{U}_e$ .
  - 7:   **Rotated non-equilibrium stress:**  $\boldsymbol{\sigma}'_{\text{neq}} = \mathbf{R}_e^T \boldsymbol{\sigma}_{\text{neq}} \mathbf{R}_e$ .
  - 8:   **Viscous update:**  $\tau_{\text{neq}} = \|\text{dev}[\boldsymbol{\sigma}'_{\text{neq}}]\|_F$ ; compute  $\dot{\varepsilon}^v$  from Eq. (12);  $\bar{\mathbf{D}}^v = \frac{\dot{\varepsilon}^v}{\tau_{\text{neq}}} \text{dev}[\boldsymbol{\sigma}'_{\text{neq}}]$ ;  $\bar{\mathbf{F}}_{\text{new}}^v = \exp(\Delta t \bar{\mathbf{D}}^v) \bar{\mathbf{F}}^v$ .
  - 9:   **Viscoplastic update:**  $\tau_{\text{tot}} = \|\text{dev}[\boldsymbol{\sigma}]\|_F$ ;
  - 10:   **if**  $\tau_{\text{tot}} \geq \sigma_0$  **then**
  - 11:     compute  $\dot{\varepsilon}^{\text{VP}}$  from Eq. (17);  $\bar{\mathbf{D}}^{\text{VP}} = \frac{\dot{\varepsilon}^{\text{VP}}}{\tau_{\text{tot}}} \text{dev}[\boldsymbol{\sigma}]$ ;  $\bar{\mathbf{F}}_{\text{new}}^{\text{VP}} = \exp(\Delta t \bar{\mathbf{D}}^{\text{VP}}) \bar{\mathbf{F}}^{\text{VP}}$ .
  - 12:   **else**  $\bar{\mathbf{F}}_{\text{new}}^{\text{VP}} = \bar{\mathbf{F}}^{\text{VP}}$ .
  - 13:   **end if**
  - 14:   **Convergence:**  $\Delta^v = \|\bar{\mathbf{F}}_{\text{new}}^v - \bar{\mathbf{F}}^v\|_F$ ,  $\Delta^{\text{VP}} = \|\bar{\mathbf{F}}_{\text{new}}^{\text{VP}} - \bar{\mathbf{F}}^{\text{VP}}\|_F$ .
  - 15:   **if**  $\Delta^v + \Delta^{\text{VP}} < \varepsilon_{\text{tol}}$  **then**
  - 16:      $\bar{\mathbf{F}}_{n+1}^v \leftarrow \bar{\mathbf{F}}_{\text{new}}^v$ ,  $\bar{\mathbf{F}}_{n+1}^{\text{VP}} \leftarrow \bar{\mathbf{F}}_{\text{new}}^{\text{VP}}$ , **converged** = true.
  - 17:   **else**  $\bar{\mathbf{F}}^v \leftarrow \bar{\mathbf{F}}_{\text{new}}^v$ ,  $\bar{\mathbf{F}}^{\text{VP}} \leftarrow \bar{\mathbf{F}}_{\text{new}}^{\text{VP}}$ .
  - 18:   **end if**
  - 19: **end while**
- 

The non-equilibrium stress is rotated to the intermediate configuration to ensure objectivity of the viscous flow rule [59]:

$$\boldsymbol{\sigma}'_{\text{neq}} = \mathbf{R}_e^T \boldsymbol{\sigma}_{\text{neq}} \mathbf{R}_e. \quad (22)$$

Upon convergence the algorithm satisfies  $\det(\bar{\mathbf{F}}_{n+1}^v) = \det(\bar{\mathbf{F}}_{n+1}^{vp}) = 1$  exactly and delivers a stress state fully consistent with both evolution equations at  $t_{n+1}$ .

### 2.3. Helmholtz free energy and stress response

The Helmholtz free energy density is additively decomposed into equilibrium, non-equilibrium, and volumetric parts [60]:

$$\rho_0 \psi(\bar{\mathbf{B}}^{ve}, \bar{\mathbf{B}}^e, J, \phi) = g(\phi) [\psi_{\text{eq}}(\bar{\mathbf{B}}^{ve}) + \psi_{\text{neq}}(\bar{\mathbf{B}}^e)] + g(\phi) \langle \psi_{\text{vol}}(J) \rangle_+ + \langle \psi_{\text{vol}}(J) \rangle_-, \quad (23)$$

where  $g(\phi)$  is the energetic degradation function coupling the free energy to the phase-field variable  $\phi \in [0, 1]$ .  $\langle \cdot \rangle_+ = \psi_{\text{vol}}$  if  $J \geq 1$  and zero otherwise, and  $\langle \cdot \rangle_- = \psi_{\text{vol}}$  if  $J < 1$  and zero otherwise. This tension–compression asymmetry prevents spurious crack nucleation under compressive loading while retaining both equilibrium and non-equilibrium deviatoric contributions as drivers of fracture. Physical consistency requires

$$g(0) = 1, \quad g(1) = 0, \quad g'(\phi) \leq 0, \quad g'(1) = 0. \quad (24)$$

The standard quadratic form satisfying these conditions is adopted:

$$g(\phi) = (1 - \phi)^2 + k, \quad (25)$$

where  $k \ll 1$  is a small residual stiffness parameter introduced to prevent ill-conditioning at fully damaged integration points [23].

The equilibrium and non-equilibrium free energies account for contributions from both the epoxy matrix and from each of the  $N_f$  carbon fiber families. Following [3], these are written as weighted sums over the fiber families:

$$\rho_0 \psi_{\text{eq}} = \sum_{i=1}^{N_f} v_f^{(i)} [\psi_{\text{eq}}^{\text{matrix}}(\bar{\mathbf{B}}^{ve}) + \psi_{\text{eq}}^{\text{fiber}(i)}(\bar{\mathbf{C}}^{ve}, \mathbf{a}_0^{(i)})], \quad (26)$$

$$\rho_0 \psi_{\text{neq}} = \sum_{i=1}^{N_f} v_f^{(i)} [\psi_{\text{neq}}^{\text{matrix}}(\bar{\mathbf{B}}^e) + \psi_{\text{neq}}^{\text{fiber}(i)}(\bar{\mathbf{C}}^e, \mathbf{a}_0^{(i)})], \quad (27)$$

where  $v_f^{(i)}$  is the volume fraction of the  $i$ -th fiber family,  $\mathbf{a}_0^{(i)}$  is the unit reference fiber direction,  $\bar{\mathbf{C}}^{ve} = (\bar{\mathbf{F}}^{ve})^T \bar{\mathbf{F}}^{ve}$  and  $\bar{\mathbf{C}}^e = (\bar{\mathbf{F}}^e)^T \bar{\mathbf{F}}^e$  are the right Cauchy–Green tensors on each intermediate configuration, and  $\rho_0$  is the reference mass density. The epoxy matrix is modeled by a neo-Hookean hyperelastic potential:

$$\psi_{\text{eq/neq}}^{\text{matrix}} = \frac{1}{2} \mu_{\text{eq/neq}} (\text{tr}[\bar{\mathbf{B}}^{ve/e}] - 3), \quad (28)$$

where  $\mu_{\text{eq}}$  and  $\mu_{\text{neq}}$  are respectively the equilibrium and non-equilibrium shear moduli of the matrix, captured using a modified Kitagawa model [61]:

$$\mu_{\text{eq}}(\theta) = \mu_{\text{eq}}^0 [2 - \exp(\alpha_\theta(\theta - \theta_0))], \quad (29)$$

$$\mu_{\text{neq}}(\theta) = \mu_{\text{neq}}^0 [2 - \exp(\alpha_\theta(\theta - \theta_0))], \quad (30)$$

where  $\mu_{\text{eq}}^0$  and  $\mu_{\text{neq}}^0$  are reference shear moduli at room temperature  $\theta_0$  and dry condition, and  $\alpha_\theta$  is a temperature sensitivity parameter.

The carbon fiber contribution for each family is described by a strain energy function that captures the coupled response of fiber stretching and fiber–matrix shear interaction [3]:

$$\begin{aligned} \psi_{\text{fiber}}^{(i)} = \frac{1}{2} \mu & \left[ (v_m + v_f^{(i)} f(\bar{I}_4^{(i)})) \left( \bar{I}_4^{(i)} + 2 \left( \bar{I}_4^{(i)} \right)^{-1/2} - 3 \right) \right. \\ & + g_1 \left( \bar{I}_4^{(i)} \right) \left( \bar{I}_5^{(i)} - \left( \bar{I}_4^{(i)} \right)^2 \right) \left( \bar{I}_4^{(i)} \right)^{-1} \\ & \left. + g_2 \left( \bar{I}_4^{(i)} \right) \left( \bar{I}_1 - \left( \bar{I}_5^{(i)} + 2 \left( \bar{I}_4^{(i)} \right)^{1/2} \right) \left( \bar{I}_4^{(i)} \right)^{-1} \right) \right], \quad (31) \end{aligned}$$

where  $v_m = 1 - \sum_{i=1}^{N_f} v_f^{(i)}$  is the matrix volume fraction,  $\mu$  stands for either  $\mu_{\text{eq}}$  or  $\mu_{\text{neq}}$  as appropriate, and the fiber invariants are

$$\bar{I}_4^{(i)} = \mathbf{a}_0^{(i)} \cdot \bar{\mathbf{C}} \mathbf{a}_0^{(i)}, \quad (32)$$

$$\bar{I}_5^{(i)} = \mathbf{a}_0^{(i)} \cdot \bar{\mathbf{C}}^2 \mathbf{a}_0^{(i)}, \quad (33)$$

representing the squared fiber stretch and a higher-order kinematic invariant, respectively.

The stiffening functions  $f$ ,  $g_1$ , and  $g_2$  in Eq. (31) are:

$$f(\bar{I}_4) = a_1 + a_2 \exp[a_3(\bar{I}_4 - 1)], \quad (34)$$

$$g_1(\bar{I}_4) = \frac{(1 + v_f^{(i)})f(\bar{I}_4) + (1 - v_f^{(i)})}{(1 - v_f^{(i)})f(\bar{I}_4) + 1 + v_f^{(i)}}, \quad (35)$$

$$g_2(\bar{I}_4) = \frac{(1 + 0.4v_f^{(i)})f(\bar{I}_4) + 0.4(1 - v_f^{(i)})}{(1 - v_f^{(i)})f(\bar{I}_4) + 0.4 + v_f^{(i)}}, \quad (36)$$

where  $a_1$ ,  $a_2$ , and  $a_3$  are material constants calibrated from uniaxial tension data of the carbon fiber/epoxy system.

The volumetric free energy is defined as

$$\rho_0 \psi_{\text{vol}} = \frac{1}{2} k_v \left( \frac{J_m^2 - 1}{2} - \ln J_m \right), \quad (37)$$

with the bulk modulus  $k_v = k_v^0$  taken as the reference value at room temperature.

It should be noted that the left Cauchy–Green tensor  $\bar{\mathbf{B}}$  is used for the isotropic matrix contributions (defined in the current configuration), while the right Cauchy–Green tensor  $\bar{\mathbf{C}}$  is employed for the fiber contributions because the fiber invariants in Eqs. (32) and (33) are expressed in the reference configuration.

The total Cauchy stress follows from the free energy by standard thermodynamic arguments:

$$\boldsymbol{\sigma} = g(\phi) (\boldsymbol{\sigma}_{\text{dev}} + \langle \boldsymbol{\sigma}_{\text{vol}} \rangle_+) + \langle \boldsymbol{\sigma}_{\text{vol}} \rangle_-, \quad (38)$$

where  $\langle \boldsymbol{\sigma}_{\text{vol}} \rangle_+$  is the volumetric stress when  $J \geq 1$  and zero otherwise, and  $\langle \boldsymbol{\sigma}_{\text{vol}} \rangle_-$  is the volumetric stress when  $J < 1$  and zero otherwise. Also, the deviatoric and volumetric contributions are given by

$$\boldsymbol{\sigma}_{\text{dev}} = J^{-1} \sum_{i=1}^{N_f} v_f^{(i)} [\boldsymbol{\sigma}_{\text{matrix}} + \boldsymbol{\sigma}_{\text{fiber}}^{(i)}], \quad (39)$$

$$\boldsymbol{\sigma}_{\text{vol}} = \frac{1}{2} k_v J^{-1} \left( J_m - \frac{1}{J_m} \right) \mathbf{I}. \quad (40)$$

The matrix stress is

$$\boldsymbol{\sigma}_{\text{matrix}} = \mu_{\text{eq}} \text{dev}[\bar{\mathbf{B}}^{\text{ve}}] + \mu_{\text{neq}} \text{dev}[\bar{\mathbf{B}}^e]. \quad (41)$$

The fiber stress for each family is derived from the strain energy function (31):

$$\begin{aligned} \boldsymbol{\sigma}_{\text{fiber}}^{(i)} = \frac{2}{J} & \left[ W_1^{(i)} \text{dev}[\bar{\mathbf{B}}] + W_4^{(i)} \bar{I}_4^{(i)} (\mathbf{a} \otimes \mathbf{a} - \frac{1}{3} \mathbf{I}) \right. \\ & \left. + W_5^{(i)} \bar{I}_4^{(i)} (\mathbf{a} \otimes \bar{\mathbf{B}}\mathbf{a} + \bar{\mathbf{B}}\mathbf{a} \otimes \mathbf{a} - \frac{2}{3} \bar{I}_5^{(i)} \mathbf{I}) \right], \end{aligned} \quad (42)$$

where  $\mathbf{a} = \bar{\mathbf{F}}\mathbf{a}_0 / (J^{2/3} \bar{I}_4^{(i)})^{1/2}$  is the unit fiber direction in the current configuration, and the scalar coefficients are

$$W_1^{(i)} = \frac{1}{2} \mu g_2, \quad (43)$$

$$\begin{aligned} W_4^{(i)} = \frac{1}{2} \mu & \left[ v_f^{(i)} f'(\bar{I}_4 + 2\bar{I}_4^{-1/2} - 3) + (v_m + v_f^{(i)} f)(1 - \bar{I}_4^{-3/2}) \right. \\ & - g_1(\bar{I}_5 \bar{I}_4^{-2} + 1) + g_2(\bar{I}_5 \bar{I}_4^{-2} + \bar{I}_4^{-3/2}) \\ & \left. + \frac{\bar{I}_5 - \bar{I}_4^2}{2\bar{I}_4} g_1' + \frac{1}{2} \left( \bar{I}_1 - \frac{\bar{I}_5 + 2\bar{I}_4^{1/2}}{\bar{I}_4} \right) g_2' \right], \end{aligned} \quad (44)$$

$$W_5^{(i)} = \frac{\mu}{2\bar{I}_4} (g_1 - g_2), \quad (45)$$

where primes denote derivatives with respect to  $\bar{I}_4^{(i)}$ .

#### 2.4. Fiber orientation and principal fiber families

In SCFRP, fibers produced by injection or compression molding are distributed with a range of orientations that depend on the flow conditions during processing. A computationally efficient representation is achieved by characterizing the orientation microstructure through a second-order orientation tensor:

$$\mathbf{A} = \frac{1}{N_{\text{fibers}}} \sum_{k=1}^{N_{\text{fibers}}} \mathbf{a}_k \otimes \mathbf{a}_k, \quad (46)$$

where  $\mathbf{a}_k$  is the unit direction of the  $k$ -th fiber and  $N_{\text{fibers}}$  is the total number of fibers. The tensor  $\mathbf{A}$  is symmetric and positive semi-definite, and its eigenvalues encode the degree of alignment. Eigenvalue decomposition of  $\mathbf{A}$  yields

$$\mathbf{A} = \sum_{i=1}^{n_{\text{dim}}} \lambda_i \mathbf{n}_i \otimes \mathbf{n}_i, \quad (47)$$

where  $\lambda_i$  and  $\mathbf{n}_i$  are the eigenvalues and orthonormal eigenvectors, and  $n_{\text{dim}}$  is the spatial dimension. The eigenvalues satisfy  $\sum_i \lambda_i = 1$  and represent the relative concentration of fibers along each principal direction. This decomposition maps the continuous orientation distribution onto a small set of discrete fiber families: the principal direction of the  $i$ -th family is  $\mathbf{a}_0^{(i)} = \mathbf{n}_i$  and its effective volume fraction is

$$v_f^{(i)} = v_f \cdot \frac{\lambda_i}{\sum_{j=1}^{N_f} \lambda_j}, \quad (48)$$

which ensures conservation of the total fiber content:

$$\sum_{i=1}^{N_f} v_f^{(i)} = v_f, \quad (49)$$

and the matrix volume fraction follows as

$$v_m = 1 - v_f. \quad (50)$$

The orientation tensor  $\mathbf{A}$  serves two purposes in the present framework. In the mechanical constitutive model it determines the principal fiber directions and their weight fractions entering the free energy expressions (26)–(27). In the anisotropic phase-field formulation it enters the gradient energy tensor  $\hat{\mathbf{A}}$  controlling the directional crack resistance (Section 3). Crucially, the same tensor also defines the anisotropic conductivity of the carbon fiber network, making the orientation decomposition the common thread connecting the mechanical, fracture, and electrical sub-problems (Section 4).

### 3. Phase-field model at finite deformation

The constitutive model of Section 2 is embedded within a variational phase-field fracture framework to predict crack nucleation and propagation in SCFRP composites. This section presents the governing equations for the coupled displacement–phase-field problem at finite deformation, the energy-based crack driving force, the weak form and finite element (FE) discretization, and the numerical scheme for the consistent spatial tangent modulus. The electric field governing equation, which completes the three-field multiphysics problem, is introduced in Section 4.

#### 3.1. Governing equations

Let  $\Omega_t \subset \mathbb{R}^{n_{\text{dim}}}$  be the deformed body at time  $t$  with boundary  $\Gamma_t$ . The strong form of the coupled boundary value problem for the displacement field  $\mathbf{u}$  and phase-field variable  $\phi \in [0, 1]$  reads

$$\nabla_{\mathbf{x}} \cdot \boldsymbol{\sigma} + \mathbf{b} = \mathbf{0} \quad \text{in } \Omega_t, \quad (51)$$

$$\boldsymbol{\sigma} \cdot \mathbf{n} = \bar{\mathbf{t}} \quad \text{on } \Gamma_t, \quad (52)$$

$$\frac{G_c}{l_0} \phi - G_c l_0 \nabla_{\mathbf{x}} \cdot (\hat{\mathbf{A}} \cdot \nabla_{\mathbf{x}} \phi) = -g'(\phi) \mathcal{H} \quad \text{in } \Omega_t, \quad (53)$$

$$\nabla_{\mathbf{x}} \phi \cdot \mathbf{n} = 0 \quad \text{on } \Gamma_t, \quad (54)$$

where  $\boldsymbol{\sigma}$  is the Cauchy stress given by Eq. (38),  $\mathbf{b}$  is the body force per unit current volume,  $\mathbf{n}$  is the outward unit normal on  $\Gamma_t$ ,  $\bar{\mathbf{t}}$  is the prescribed traction,  $G_c$  is the critical energy release rate, and  $l_0$  is the length scale parameter governing the width of the diffuse crack band.

The tensor  $\hat{\mathbf{A}}$  in Eq. (53) introduces directional dependence into the crack resistance and is defined as [22]

$$\hat{\mathbf{A}} = \mathbf{I} + \hat{\alpha} \mathbf{A}, \quad (55)$$

where  $\mathbf{A}$  is the fiber orientation tensor of Eq. (46) and  $\hat{\alpha} \geq 0$  is a dimensionless anisotropy parameter. Setting  $\hat{\alpha} = 0$  recovers the isotropic phase-field model. For  $\hat{\alpha} > 0$ , the gradient energy term in Eq. (53) penalizes crack gradients along fiber directions more strongly than across them, so that crack propagation perpendicular to the fiber axis — which must sever the load-bearing fibers — requires more energy than propagation parallel to them. The magnitude of the penalty grows with  $\hat{\alpha}$  and with the eigenvalues of  $\mathbf{A}$ , i.e., with the degree of fiber alignment. The critical energy release rate  $G_c$  represents the energy required to create a

unit area of crack surface and is calibrated from experimental fracture tests on the CF/epoxy system.

### 3.2. Energy-based crack driving force

A history-field approach is adopted to account for the irreversibility of crack growth and to incorporate both elastic and viscous energy contributions into the fracture driving force [23]. The crack driving force  $\mathcal{H}$  is defined as the maximum strain energy density reached over the entire loading history:

$$\mathcal{H}(t) = \max_{\tau \in [0, t]} \mathcal{Y}(\tau), \quad (56)$$

where the instantaneous energy density available to drive fracture is

$$\mathcal{Y} = \psi_{\text{eq}}(\bar{\mathbf{B}}^{\text{ve}}) + \psi_{\text{neq}}(\bar{\mathbf{B}}^e) + \langle \psi_{\text{vol}}(J) \rangle_+, \quad (57)$$

with the positive-part operator  $\langle \cdot \rangle_+ = (\cdot + |\cdot|)/2$ . The volumetric contribution is admitted only in tension:

$$\langle \psi_{\text{vol}}(J) \rangle_+ = \begin{cases} \psi_{\text{vol}}(J) & \text{if } J \geq 1, \\ 0 & \text{if } J < 1, \end{cases} \quad (58)$$

where  $J \geq 1$  signifies volume expansion (tension) and  $J < 1$  volume contraction (compression). This split prevents spurious crack growth under compressive loading while retaining both equilibrium and non-equilibrium free energy contributions as drivers of fracture — a physically important feature for viscoelastic-viscoplastic materials in which viscous energy storage can represent a significant fraction of the total stored energy.

The history variable is updated at each time step as

$$\mathcal{H}^{n+1} = \max(\mathcal{H}^n, \mathcal{Y}^{n+1}), \quad (59)$$

ensuring that  $\phi$  can only increase monotonically, consistent with thermodynamic irreversibility of fracture.

### 3.3. Weak form and finite element discretization

Multiplying Eqs. (51) and (53) by admissible test functions  $\boldsymbol{\eta}_u \in H_0^1(\Omega)$  and  $\eta_\phi \in H_0^1(\Omega)$ , integrating over  $\Omega_t$ , and applying the divergence theorem yields the weak form:

$$\int_{\Omega_t} \boldsymbol{\sigma} : \nabla_{\mathbf{x}} \boldsymbol{\eta}_u \, dv - \int_{\Omega_t} \rho_t \mathbf{b} \cdot \boldsymbol{\eta}_u \, dv - \int_{\Gamma_t} \bar{\mathbf{t}} \cdot \boldsymbol{\eta}_u \, da = 0, \quad (60)$$

$$\int_{\Omega_t} \left[ J^{-1} g'(\phi) \mathcal{H} \eta_\phi + J^{-1} \frac{G_c}{l_0} \phi \eta_\phi + J^{-1} G_c l_0 \nabla_{\mathbf{x}} \phi \cdot \hat{\mathbf{A}} \cdot \nabla_{\mathbf{x}} \eta_\phi \right] dv = 0. \quad (61)$$

### 3.4. Consistent incremental-iterative scheme

Under the assumption of deformation-independent external loading, Eqs. (60) and (61) are cast as residual equations in terms of internal and external nodal force vectors:

$$\mathbf{r}^u = \mathbf{f}_{\text{int}}^u - \mathbf{f}_{\text{ext}}^u = \mathbf{0}, \quad (62)$$

$$\mathbf{r}^\phi = \mathbf{f}_{\text{int}}^\phi - \mathbf{f}_{\text{ext}}^\phi = \mathbf{0}, \quad (63)$$

where

$$\mathbf{f}_{\text{int}}^u = \int_{\Omega_t} \boldsymbol{\sigma} : \nabla_x \boldsymbol{\eta}_u \, dv, \quad (64)$$

$$\mathbf{f}_{\text{ext}}^u = \int_{\Omega} \rho_t \mathbf{b} \cdot \boldsymbol{\eta}_u \, dv + \int_{\Gamma_t} \bar{\mathbf{t}} \cdot \boldsymbol{\eta}_u \, da, \quad (65)$$

$$\mathbf{f}_{\text{int}}^\phi = \int_{\Omega_t} \left[ J^{-1} g'(\phi) \mathcal{H} \eta_\phi + J^{-1} \frac{G_c}{l_0} \phi \eta_\phi + J^{-1} G_c l_0 \nabla_x \phi \cdot \hat{\mathbf{A}} \cdot \nabla_x \eta_\phi \right] dv, \quad (66)$$

$$\mathbf{f}_{\text{ext}}^\phi = \mathbf{0}. \quad (67)$$

Newton–Raphson linearization of the residuals at iteration  $i + 1$  gives

$$\mathbf{r}_{i+1}^u = \mathbf{r}_i^u + \Delta \mathbf{r}^u = \mathbf{0}, \quad (68)$$

$$\mathbf{r}_{i+1}^\phi = \mathbf{r}_i^\phi + \Delta \mathbf{r}^\phi = \mathbf{0}, \quad (69)$$

where

$$\Delta \mathbf{r}^u = D_u \mathbf{r}_i^u \cdot \Delta \mathbf{u} + D_\phi \mathbf{r}_i^u \cdot \Delta \phi, \quad (70)$$

$$\Delta \mathbf{r}^\phi = D_u \mathbf{r}_i^\phi \cdot \Delta \mathbf{u} + D_\phi \mathbf{r}_i^\phi \cdot \Delta \phi. \quad (71)$$

Carrying out the linearization of Eqs. (60) and (61) in the spatial configuration yields

$$\begin{aligned} \int_{\Omega_t} (\nabla_x \Delta \mathbf{u} \cdot \boldsymbol{\sigma} \cdot \nabla_x \boldsymbol{\eta}_u + \nabla_x^s \boldsymbol{\eta}_u : \hat{\mathbf{c}} : \nabla_x^s \Delta \mathbf{u}) dv \\ + \int_{\Omega_t} \nabla_x^s \boldsymbol{\eta}_u : D_\phi \boldsymbol{\sigma} \cdot \Delta \phi \, dv = \mathbf{f}_{\text{ext}}^u - \mathbf{f}_{\text{int},i}^u, \end{aligned} \quad (72)$$

and

$$\begin{aligned} \int_{\Omega_t} J^{-1} g'(\phi) 2 \frac{\partial \mathcal{H}}{\partial \mathbf{g}} \cdot \nabla_x \Delta \mathbf{u} \, \eta_\phi \, dv \\ + \int_{\Omega_t} \left[ J^{-1} g''(\phi) \mathcal{H} \Delta \phi \, \eta_\phi + J^{-1} \frac{G_c}{l_0} \Delta \phi \, \eta_\phi + J^{-1} G_c l_0 \nabla_x \Delta \phi \cdot \hat{\mathbf{A}} \cdot \nabla_x \eta_\phi \right] dv \\ = \mathbf{f}_{\text{ext}}^\phi - \mathbf{f}_{\text{int},i}^\phi, \end{aligned} \quad (73)$$

where  $\hat{\mathbf{c}}$  is the spatial tangent modulus (the Piola push-forward of  $\partial \mathbf{S} / \partial \mathbf{C}$ , with  $\mathbf{S}$  the second Piola–Kirchhoff stress), and  $\partial(\cdot) / \partial \mathbf{g} = \mathbf{F} \partial(\cdot) / \partial \mathbf{C} \mathbf{F}^T$ .

### 3.5. Finite element formulation

The linearized Eqs. (72) and (73) are assembled into the two-field system

$$\begin{bmatrix} \mathbf{K}_i^{uu} & \mathbf{K}_i^{u\phi} \\ \mathbf{K}_i^{\phi u} & \mathbf{K}_i^{\phi\phi} \end{bmatrix} \begin{bmatrix} \Delta \mathbf{u}_{i+1} \\ \Delta \phi_{i+1} \end{bmatrix} = \begin{bmatrix} \mathbf{f}_{\text{ext}}^u \\ \mathbf{f}_{\text{ext}}^\phi \end{bmatrix} - \begin{bmatrix} \mathbf{f}_{\text{int},i}^u \\ \mathbf{f}_{\text{int},i}^\phi \end{bmatrix}, \quad (74)$$

with the tangent stiffness sub-matrices

$$\mathbf{K}_i^{uu} = \int_{\Omega} \mathbf{B}_u^T \hat{\mathbf{c}} \mathbf{B}_u d\Omega + \int_{\Omega} \mathbf{B}_u^T \boldsymbol{\sigma} \mathbf{B}_u d\Omega, \quad (75)$$

$$\mathbf{K}_i^{u\phi} = \int_{\Omega} \mathbf{B}_u^T \left( \frac{\partial \boldsymbol{\sigma}}{\partial \phi} \right) \mathbf{N}_\phi d\Omega, \quad (76)$$

$$\mathbf{K}_i^{\phi u} = \int_{\Omega} \mathbf{N}_\phi^T J^{-1} g'(\phi) 2 \frac{\partial \mathcal{H}}{\partial \mathbf{g}} \mathbf{B}_u d\Omega, \quad (77)$$

$$\mathbf{K}_i^{\phi\phi} = \int_{\Omega} J^{-1} \left[ \mathbf{N}_\phi^T \left( g''(\phi) \mathcal{H} + \frac{G_c}{l_0} \right) \mathbf{N}_\phi + G_c l_0 \mathbf{B}_\phi^T \hat{\mathbf{A}} \mathbf{B}_\phi \right] d\Omega, \quad (78)$$

where  $\mathbf{N}_u$  and  $\mathbf{N}_\phi$  are the shape function matrices for the displacement and phase-field, and  $\mathbf{B}_u$  and  $\mathbf{B}_\phi$  are the corresponding gradient operators. Standard isoparametric Q4 elements with  $2 \times 2$  Gauss quadrature are used for all fields. The coupled system (74) is solved using a staggered algorithm [20] in which the displacement and phase-field sub-problems are solved sequentially within each load step. After convergence of both sub-problems, the electric field equation (Section 4) is solved as a decoupled linear system, exploiting the one-way coupling from the mechanical-damage state to the electrical response.

### 3.6. Consistent tangent modulus based on the Jaumann–Zaremba rate

At finite deformation the material time derivative of the Cauchy stress is not objective under superposed rigid body motions. The Jaumann–Zaremba rate is therefore used to formulate an objective constitutive tangent:

$$\overset{\nabla}{\boldsymbol{\sigma}} = \dot{\boldsymbol{\sigma}} - \mathbf{W}\boldsymbol{\sigma} - \boldsymbol{\sigma}\mathbf{W}^T = \mathbf{C}^{\sigma J} : \mathbf{D}, \quad (79)$$

where  $\mathbf{D}$  is the rate of deformation tensor and  $\mathbf{W}$  is the spin tensor. The spatial tangent  $\hat{\mathbf{c}}$  required by the FE weak form in Eq. (75) is the Piola push-forward of the material tangent  $\partial \mathbf{S} / \partial \mathbf{C}$ :

$$\hat{\mathbf{c}} = \frac{1}{J} (\mathbf{F} \overline{\otimes} \mathbf{F}) : \frac{\partial \mathbf{S}}{\partial \mathbf{C}} : (\mathbf{F}^T \overline{\otimes} \mathbf{F}^T). \quad (80)$$

A closed-form evaluation of Eq. (80) is impractical for the complex coupled viscoelastic-viscoplastic-damage model. The Jaumann tangent  $\mathbf{C}^{\sigma J}$  is therefore computed numerically by

a forward-difference perturbation scheme [62]. A symmetric perturbation is applied to the  $(k, l)$  components of the deformation gradient:

$$\Delta \mathbf{F}_{kl} = \frac{\epsilon}{2} (\mathbf{e}_k \otimes \mathbf{e}_l \mathbf{F} + \mathbf{e}_l \otimes \mathbf{e}_k \mathbf{F}), \quad (81)$$

with  $\epsilon = 10^{-5}$ . The corresponding perturbations in the spin and rate-of-deformation tensors are

$$\Delta \mathbf{W}_{kl} = \mathbf{0}, \quad (82)$$

$$\Delta \mathbf{D}_{kl} = \frac{\epsilon}{2} (\mathbf{e}_k \otimes \mathbf{e}_l + \mathbf{e}_l \otimes \mathbf{e}_k). \quad (83)$$

Since  $\Delta \mathbf{W}_{kl} = \mathbf{0}$ , the Jaumann rate reduces to  $\Delta \boldsymbol{\sigma} = \mathbf{C}^{\sigma J} : \Delta \mathbf{D}$ , so the components of  $\mathbf{C}^{\sigma J}$  follow from

$$\hat{\mathbf{F}}_{kl} = \mathbf{F} + \Delta \mathbf{F}_{kl}, \quad (84)$$

$$\Delta \boldsymbol{\sigma} \approx \boldsymbol{\sigma}(\hat{\mathbf{F}}_{kl}) - \boldsymbol{\sigma}(\mathbf{F}), \quad (85)$$

$$\mathbf{C}_{kl}^{\sigma J} = \frac{1}{\epsilon} [\boldsymbol{\sigma}(\hat{\mathbf{F}}_{kl}) - \boldsymbol{\sigma}(\mathbf{F})]. \quad (86)$$

The procedure is summarized in Algorithm 2.

---

**Algorithm 2** Computation of the consistent spatial tangent modulus.

---

1. Set perturbation parameter  $\epsilon = 10^{-5}$ .
  2. Evaluate baseline Cauchy stress  $\boldsymbol{\sigma}(\mathbf{F})$  using the constitutive model of Section 2.
  4. **for**  $k = 1, \dots, n_{\text{dim}}$  **do**
  5.   **for**  $l = 1, \dots, n_{\text{dim}}$  **do**
  6.     Set  $\hat{\mathbf{F}} = \mathbf{F}$ .
  7.     Apply symmetric perturbation:  $\hat{F}_{kl} += \epsilon/2$ ,  $\hat{F}_{lk} += \epsilon/2$ .
  8.     Evaluate perturbed stress  $\boldsymbol{\sigma}(\hat{\mathbf{F}})$ .
  9.     Compute  $\Delta \boldsymbol{\sigma} = \boldsymbol{\sigma}(\hat{\mathbf{F}}) - \boldsymbol{\sigma}(\mathbf{F})$  (Eq. (85)).
  10.     Store columns  $\mathbf{C}_{kl}^{\sigma J}$  and  $\mathbf{C}_{lk}^{\sigma J}$  using Eq. (86).
  11.   **end**
  12. **end**
  13. Store  $\mathbf{C}^{\sigma J}$  in Voigt notation.
- 

The spatial tangent  $\hat{\mathbf{c}}$  is then recovered from the Jaumann tangent  $\mathbf{C}^{\sigma J}$  by the standard Jaumann-to-Truesdell correction [10]:

$$\hat{\mathbf{c}} = \mathbf{C}^{\sigma J} - \frac{1}{2} (\mathbf{I} \overline{\otimes} \boldsymbol{\sigma} + \mathbf{I} \underline{\otimes} \boldsymbol{\sigma} + \boldsymbol{\sigma} \overline{\otimes} \mathbf{I} + \boldsymbol{\sigma} \underline{\otimes} \mathbf{I}) + \boldsymbol{\sigma} \otimes \mathbf{I}. \quad (87)$$

The resulting  $\hat{\mathbf{c}}$  is symmetrized to remove floating-point noise, since the theoretical major symmetry of a potential-based tangent is satisfied exactly only after the Jaumann correction is applied. This purely numerical differentiation strategy avoids the derivation of closed-form tangent expressions for the complex coupled constitutive model while delivering the quadratic convergence rate of the Newton–Raphson iterations.

#### 4. Piezoresistive model

This section introduces the governing equation for the electric potential, derives the damage-coupled piezoresistive conductivity tensor, and defines the resistance-based self-sensing observable. Two physically distinct piezoresistive mechanisms operate simultaneously under mechanical loading. The first is a geometric-kinematic mechanism. Deformation rotates and stretches the fibers, altering the effective conduction path lengths and the contact geometry between neighboring fibers. The second is a damage-driven mechanism: matrix cracking and fiber–matrix debonding sever conductive pathways irreversibly, causing resistance to increase in proportion to the accumulation of phase-field damage  $\phi$ . The framework developed below captures both mechanisms within a single continuum conductivity tensor.

##### 4.1. Governing equation for the electric potential

Under the quasi-static assumption with no free bulk charge, the electric potential  $\phi_e$  satisfies the steady-state charge conservation equation in the deformed configuration  $\Omega_t$ :

$$\nabla_{\mathbf{x}} \cdot (\hat{\boldsymbol{\sigma}}_{\text{eff}} \cdot \nabla_{\mathbf{x}} \phi_e) = 0 \quad \text{in } \Omega_t, \quad (88)$$

with Dirichlet boundary conditions

$$\phi_e = V_{\text{app}} \quad \text{on } \Gamma_V, \quad \phi_e = 0 \quad \text{on } \Gamma_0, \quad (89)$$

and homogeneous Neumann conditions  $(\hat{\boldsymbol{\sigma}}_{\text{eff}} \cdot \nabla_{\mathbf{x}} \phi_e) \cdot \mathbf{n} = 0$  on the remaining boundary. Here  $\Gamma_V$  is the voltage electrode,  $\Gamma_0$  is the ground electrode,  $V_{\text{app}}$  is the applied voltage, and  $\hat{\boldsymbol{\sigma}}_{\text{eff}}$  is the effective electrical conductivity tensor derived in Section 4.2. The electric current density is

$$\mathbf{J} = -\hat{\boldsymbol{\sigma}}_{\text{eff}} \cdot \nabla_{\mathbf{x}} \phi_e. \quad (90)$$

Eq. (88) is linear in  $\phi_e$  for fixed  $\hat{\boldsymbol{\sigma}}_{\text{eff}}$ , so the electric field sub-problem reduces to a single linear system solve once the mechanical and phase-field fields have converged.

#### 4.2. Damage-coupled piezoresistive conductivity tensor

The undamaged, unstrained effective conductivity tensor at a material point is assembled by superimposing the isotropic matrix contribution and the transversely isotropic fiber contribution from each principal fiber family  $i = 1, \dots, N_f$ :

$$\hat{\boldsymbol{\sigma}}_0 = \sigma_m \mathbf{I} + \sum_{i=1}^{N_f} v_f^{(i)} \left[ \sigma_{\parallel}^{(i)} \mathbf{a}^{(i)} \otimes \mathbf{a}^{(i)} + \sigma_{\perp}^{(i)} (\mathbf{I} - \mathbf{a}^{(i)} \otimes \mathbf{a}^{(i)}) \right]. \quad (91)$$

The principal fiber directions  $\mathbf{a}^{(i)}$  in Eq. (91) coincide with the eigenvectors  $\mathbf{n}_i$  of the orientation tensor  $\mathbf{A}$  (Eq. (47)), and the associated volume fractions  $v_f^{(i)}$  are determined by Eq. (48). Thus,  $\hat{\boldsymbol{\sigma}}_0$  inherits its anisotropy directly from  $\mathbf{A}$ .

The tensor structure in Eq. (91) is transversely isotropic about  $\mathbf{a}^{(i)}$ . The projection  $\mathbf{a}^{(i)} \otimes \mathbf{a}^{(i)}$  carries conductivity  $\sigma_{\parallel}^{(i)}$  along the fiber axis, while the complementary projector  $(\mathbf{I} - \mathbf{a}^{(i)} \otimes \mathbf{a}^{(i)})$  carries conductivity  $\sigma_{\perp}^{(i)}$  in all directions transverse to the fiber. This representation is fully consistent with the fiber family decomposition of Section 2.4.

The strain-dependent axial and transverse conductivities follow a linear piezoresistive law [51]:

$$\sigma_{\parallel}^{(i)} = \sigma_{\parallel}^0 (1 - \text{GF}_{\parallel} \varepsilon_{\parallel}^{(i)}), \quad (92)$$

$$\sigma_{\perp}^{(i)} = \sigma_{\perp}^0 (1 - \text{GF}_{\perp} \varepsilon_{\perp}^{(i)}), \quad (93)$$

where  $\text{GF}_{\parallel}$  and  $\text{GF}_{\perp}$  are the longitudinal and transverse gauge factors, respectively. Mechanical deformation changes the intrinsic conductivity of each fiber family. Therefore, the fiber-parallel and fiber-transverse strain scalars for the  $i$ -th family are

$$\varepsilon_{\parallel}^{(i)} = \mathbf{a}_0^{(i)} \cdot \mathbf{E} \mathbf{a}_0^{(i)}, \quad (94)$$

$$\varepsilon_{\perp}^{(i)} = \frac{1}{2} (\text{tr}[\mathbf{E}] - \varepsilon_{\parallel}^{(i)}). \quad (95)$$

Progressive matrix cracking and fiber–matrix debonding sever the conductive carbon fiber network, degrading the macroscopic conductivity in proportion to the phase-field damage variable  $\phi$ . This is modeled by multiplying the conductivity tensor by a scalar degradation function:

$$\hat{\boldsymbol{\sigma}}_{\text{eff}} = h_e(\phi) \hat{\boldsymbol{\sigma}}_0, \quad (96)$$

where

$$h_e(\phi) = (1 - \phi)^p + k_e. \quad (97)$$

The exponent  $p$  controls the rate at which conductivity degrades as damage accumulates, and  $k_e$  is a small residual conductivity retained for numerical stability at fully damaged points. Setting  $p = 2$  reproduces the same quadratic form as the mechanical degradation function  $g(\phi) = (1 - \phi)^2 + k$  (Eq. (25)), enforcing consistent degradation kinetics.

The primary structural health monitoring observable is the specimen-level electrical resistance  $R$ , obtained from the total current  $I$  flowing through the voltage electrode:

$$I = \int_{\Gamma_V} \mathbf{J} \cdot \mathbf{n} \, da, \quad (98)$$

$$R = \frac{V_{\text{app}}}{I}. \quad (99)$$

The normalized conductivity, defined as the ratio of the current resistance  $R$  to the initial undamaged resistance  $R_0$ , provides a dimensionless self-sensing indicator bounded between 0 and 1:

$$\frac{\sigma}{\sigma_0} = \frac{R_0}{R}, \quad (100)$$

where  $R_0$  is the resistance computed at the first load step before any deformation or damage. The normalized conductivity starts at unity in the undamaged composite and decreases monotonically toward zero as fracture progresses.

#### 4.3. Weak form and finite element discretization

Multiplying Eq. (88) by a test function  $\eta_e \in H_0^1(\Omega_t)$ , integrating over  $\Omega_t$ , and applying the divergence theorem yields the weak form of the electric field problem:

$$\int_{\Omega_t} \nabla_{\mathbf{x}} \eta_e \cdot \hat{\boldsymbol{\sigma}}_{\text{eff}} \cdot \nabla_{\mathbf{x}} \phi_e \, dv = 0. \quad (101)$$

The discretized nodal electric potentials  $\phi_e$  are interpolated as  $\phi_e \approx \mathbf{N}_e \boldsymbol{\phi}_e$ , where  $\mathbf{N}_e$  collects the element shape functions. The element conductivity matrix is

$$\mathbf{K}_e^{ee} = \int_{\Omega_t^e} \mathbf{B}_e^T \hat{\boldsymbol{\sigma}}_{\text{eff}} \mathbf{B}_e \, dv, \quad (102)$$

where  $\mathbf{B}_e = \nabla_{\mathbf{x}} \mathbf{N}_e$  is the electric potential gradient matrix evaluated in the current configuration. The conductivity tensor  $\hat{\boldsymbol{\sigma}}_{\text{eff}}$  is evaluated at each Gauss point using Eq. (96) with the converged  $\mathbf{F}$  and  $\phi$  fields. The global system  $\mathbf{K}^{ee} \boldsymbol{\phi}_e = \mathbf{f}^e$  is linear and is solved in a single step. The element load vector  $\mathbf{f}_e^e$  arises solely from the Dirichlet boundary conditions on the electrode surfaces.

The mechanical, phase-field, and electric field sub-problems are coupled in a one-way cascade. Deformation and damage govern the conductivity, but the electric field does not affect the mechanical or fracture response. This one-way coupling is exploited by solving the three fields sequentially within each load step, as summarized in Algorithm 3.

---

**Algorithm 3** Staggered solution algorithm for the three-field coupled problem.

---

- 1: **Given:** displacement increment  $\Delta\bar{u}$ ,  $\Delta t$ ,  $V_{\text{app}}$ ,  $\varepsilon_{\text{tol}}$ , max. load reductions  $n_{\text{red}}$ , load reduction factor  $k_{\text{red}}$ .
  - 2: Apply  $\Delta\bar{u}$ ; initialize Newton–Raphson counter  $n_{\text{NR}} = 1$ .
  - 3: **while** simulation not complete **do**
  - 4:     **Displacement sub-problem (Newton–Raphson):**
  - 5:         Assemble  $\mathbf{K}^{uu}$  and  $\mathbf{f}_{\text{int}}^u$  (Eqs. (75), (64)).
  - 6:         Solve  $\mathbf{K}^{uu} \Delta\mathbf{u} = \mathbf{f}_{\text{ext}}^u - \mathbf{f}_{\text{int}}^u$ .
  - 7:         Update  $\bar{\mathbf{F}}_{n+1}^v$ ,  $\bar{\mathbf{F}}_{n+1}^{\text{vp}}$  via Algorithm 1.
  - 8:     **Phase-field sub-problem (Newton–Raphson):**
  - 9:         Assemble  $\mathbf{K}^{\phi\phi}$  and  $\mathbf{f}_{\text{int}}^{\phi}$  (Eqs. (78), (66)).
  - 10:         Solve  $\mathbf{K}^{\phi\phi} \Delta\phi = -\mathbf{f}_{\text{int}}^{\phi}$ .
  - 11:         Update history variable:  $\mathcal{H}^{n+1} = \max(\mathcal{H}^n, \mathcal{Y}^{n+1})$  (Eq. (59)).
  - 12:     **if**  $\|\Delta\mathbf{u}\|/\|\mathbf{u}\| \leq \varepsilon_{\text{tol}}$  **and**  $\|\Delta\phi\|/\|\phi\| \leq \varepsilon_{\text{tol}}$  **then**
  - 13:         **Electric field sub-problem (linear solve):**
  - 14:             Evaluate  $\hat{\boldsymbol{\sigma}}_{\text{eff}}$  at all Gauss points via Eq. (96).
  - 15:             Assemble  $\mathbf{K}^{ee}$  (Eq. (102)).
  - 16:             Apply BCs:  $\phi_e = V_{\text{app}}$  on  $\Gamma_V$ ,  $\phi_e = 0$  on  $\Gamma_0$ .
  - 17:             Solve  $\mathbf{K}^{ee} \phi_e = \mathbf{f}^e$ .
  - 18:             Compute  $\mathbf{J} = -\hat{\boldsymbol{\sigma}}_{\text{eff}} \nabla_{\mathbf{x}} \phi_e$  (Eq. (90)).
  - 19:             Compute  $I$  (Eq. (98)),  $R = V_{\text{app}}/I$  (Eq. (99)),  $\sigma/\sigma_0 = R_0/R$  (Eq. (100)).
  - 20:             Store  $\{u, F, \phi, R, \sigma/\sigma_0\}$ ; advance load step.
  - 21:     **else**
  - 22:         **if**  $n_{\text{NR}} \leq n_{\text{red}}$  **then**
  - 23:             Reduce  $\Delta\bar{u} \leftarrow \Delta\bar{u}/k_{\text{red}}$ ;  $\Delta t \leftarrow \Delta t/k_{\text{red}}$ ;  $n_{\text{NR}} += 1$ ; **restart step**.
  - 24:         **else terminate**.
  - 25:     **end if**
  - 26: **end if**
  - 27: **end while**
-

## 5. Structural health monitoring

The coupled phase-field and piezoresistive framework developed in the preceding sections provides the physical basis for a non-invasive structural health monitoring system: as a crack initiates and propagates under mechanical loading, the spatial distribution of the phase-field variable  $\phi$  degrades the effective conductivity tensor  $\hat{\sigma}_{\text{eff}}$  through the damage function  $h_e(\phi)$ , producing measurable changes in the inter-electrode conductances that encode the evolving damage state of the specimen. To exploit this coupling for in-service damage monitoring, an EIT configuration is adopted, following the electrode layouts employed in experimental piezoresistive studies of carbon fiber-reinforced composites [63].

The electrode arrangement is illustrated in Fig. 2. Eight patch electrodes  $E_1$ – $E_8$ , each of nominal half-width  $l_c$ , are placed at the quarter-points of the four boundary edges of the single-edge notched specimen, with two electrodes per edge. For a given injection pair, a constant voltage  $V_{\text{app}}$  is applied at the anode electrode while the cathode is held at zero potential; the remaining six electrodes act as passive voltage sensors, recording the inter-electrode potential differences that reflect the spatial distribution of  $\hat{\sigma}_{\text{eff}}$  in the interior. Cycling sequentially through all  $\binom{8}{2} = 28$  injection pairs and recording the resulting conductance

$$G_{ij}^{(n)} = \frac{1}{V_{\text{app}}} \left| \sum_{k \in \mathcal{E}_i} (\hat{\sigma}_{\text{eff}} \cdot \nabla \phi_e) \cdot \mathbf{n} \, dA \right| \quad (103)$$

at each load step yields 28 independent scalar measurements per step, assembled into the measurement vector  $\mathbf{g}^{(n)} = \{G_{ij}^{(n)}\}_{i < j} \in \mathbb{R}^{28}$ . The normalised conductance ratios  $G_{ij}^{(n)}/G_{ij}^0$ , where  $G_{ij}^0$  denotes the undamaged reference conductance measured at the start of loading, serve as the primary electrical observables: they are bounded in  $(0, 1]$ , monotonically decreasing with damage progression, and insensitive to the absolute conductivity level, which removes the dependence on fiber volume fraction and contact resistance variations between specimens. The top edge of the specimen is subjected to a prescribed displacement rate  $\dot{u} = 1$  mm/min, consistent with the quasi-static loading conditions assumed in the constitutive model.

The inverse problem seeks the current damage state from the electrical measurements alone. Two scalar global damage indicators are adopted as outputs: (1) the normalized crack length  $\tilde{a} = \ell_{\text{crack}}/W$ , obtained from the crack surface density functional

$$\ell_{\text{crack}} = \int_{\Omega} \left( \frac{\phi^2}{2l_c} + \frac{l_c}{2} |\nabla \phi|^2 \right) dV, \quad (104)$$

and (2) the normalized mechanical compliance  $\tilde{C} = C/C_0 = (u_{\text{top}}/F_{\text{top}})/C_0$ , where  $C_0$  is the undamaged reference compliance. Both quantities are continuous, monotonically increasing

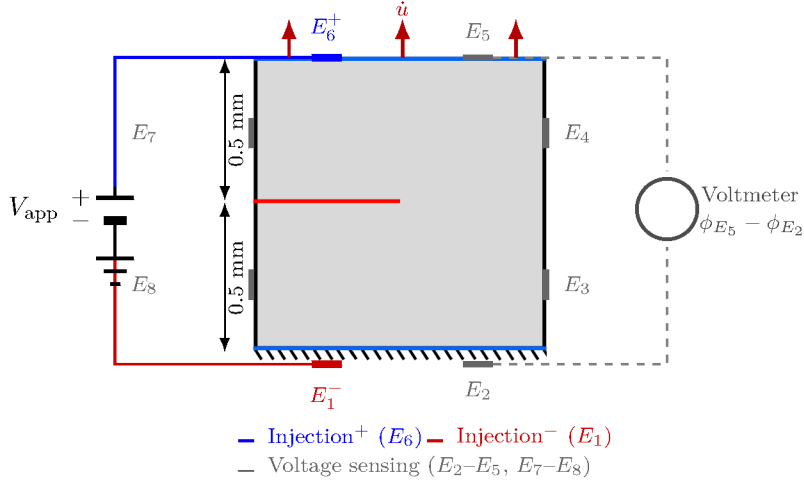


**Figure 2:** Eight-electrode EIT configuration for spatial conductivity mapping of the single-edge notched specimen. The top edge is subjected to a prescribed tensile displacement  $\dot{u} = 1$  mm/min.

functions of the damage state and are threshold-free by construction, in contrast to point-based crack tip locators that are sensitive to mesh resolution and the choice of a phase-field threshold.

The inverse mapping to be learned is therefore

$$\mathcal{F}: (A_{11}, A_{12}, v_f, \theta, \mathbf{g}^{(n)}/\mathbf{g}^0) \mapsto (\tilde{a}^{(n)}, \tilde{C}^{(n)}), \quad (105)$$

where  $A_{11}$  and  $A_{12}$  are the independent components of the second-order fiber orientation tensor  $\mathbf{A}$  (with the constraint  $A_{11} + A_{22} = 1$ ), and  $\mathbf{g}^{(n)}/\mathbf{g}^0 \in (0, 1]^{28}$  is the vector of 28 normalized conductance ratios at load step  $n$ . The microstructure descriptors ( $A_{11}, A_{12}, v_f$ ) are fixed properties of the specimen, available from manufacturing data; the conductance ratios are the sole time-varying measurements. The total input dimension is therefore  $4 + 28 = 32$ .

The mapping  $\mathcal{F}$  is nonlinear and implicitly defined through the coupled three-field problem. Its direct inversion is intractable in closed form, and iterative forward solves would be computationally prohibitive in a real-time monitoring context. The present work approximates  $\mathcal{F}$  by a feedforward ANN trained on the phase-field simulation dataset described in Section 6.2. The key advantage of the orientation tensor parameterization is that  $\mathbf{A}$  provides a continuous, physically consistent representation of the microstructure that interpolates smoothly across single-family, multi-family, and randomly oriented fiber architectures, enabling the trained model to generalize to configurations not seen during training.

The overall workflow of the phase-field-informed SHM framework is summarized in Fig. 3. The framework operates in two distinct phases. In the offline training phase, phase-field simulations are executed for a systematic set of fiber architectures, temperatures, and loading conditions, producing per-step datasets of normalized conductances  $G_{ij}^{(n)}/G_{ij}^0$ , normalised crack length  $\tilde{a}$ , and normalized compliance  $\tilde{C}$ . In the online monitoring phase, the trained model receives two inputs at each monitoring cycle: the fixed specimen descriptor  $(A_{11}, A_{12}, v_f)$  available from manufacturing data, and the 28 conductance ratios measured electrically from the eight-electrode network. The model then instantly returns estimates of the current normalized crack length  $\hat{a}^{(n)}$  and normalized compliance  $\hat{C}^{(n)}$ , enabling real-time damage tracking without any mechanical loading or measurement.

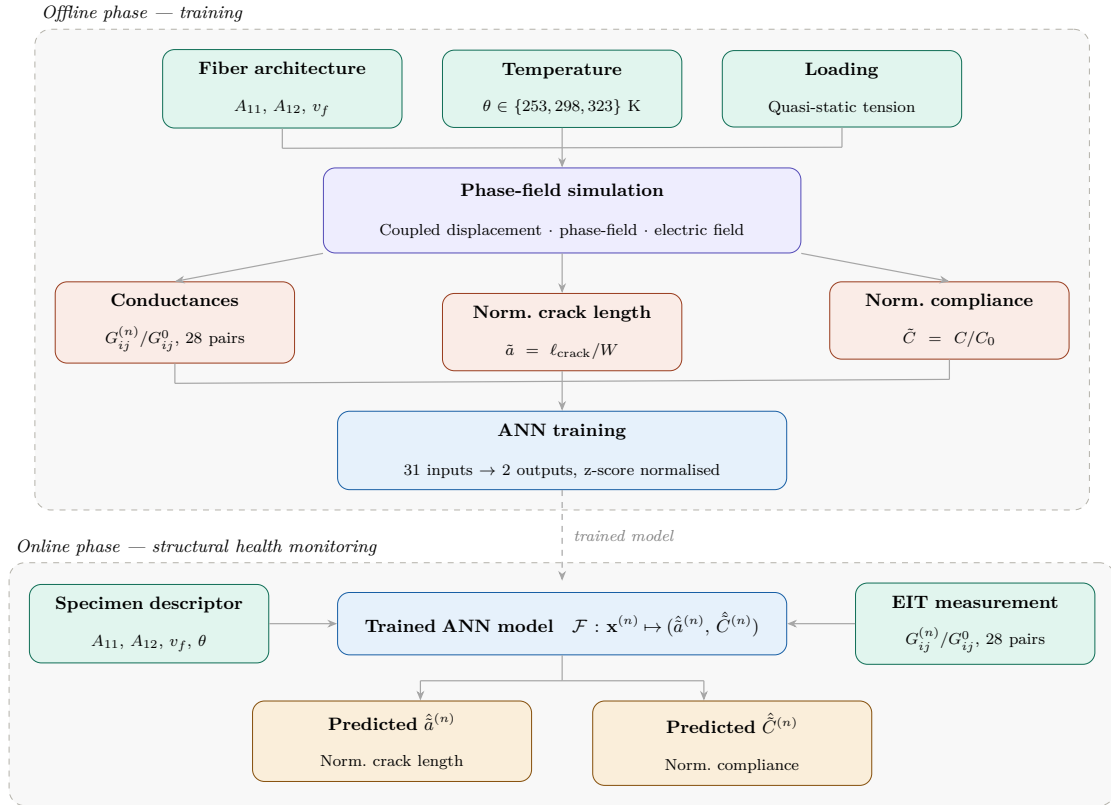


**Figure 3:** Schematic of the phase-field-informed ANN framework for SHM of SCFRP composites. Offline phase (top): phase-field simulations spanning a range of fiber architectures, temperatures, and loading conditions generate training data. Online phase (bottom): at each monitoring cycle the trained model  $\mathcal{F}$  receives the fixed specimen descriptor  $(A_{11}, A_{12}, v_f)$  and the current EIT conductance measurements, and returns real-time predictions of the normalized crack length  $\hat{a}^{(n)}$  and compliance  $\hat{C}^{(n)}$  without mechanical sensing.

## 6. Numerical simulations

### 6.1. Phase-field simulations

A comprehensive set of numerical simulations is presented to demonstrate the predictive capability of the proposed three-field framework and to elucidate the interplay between anisotropic viscoelastic-viscoplastic fracture and damage-induced piezoresistive response in SCFRP composites. All simulations examine CF/epoxy composites under quasi-static tensile loading. The material parameters for the constitutive model, the phase-field fracture formulation, and the piezoresistive electrical model are summarized in Table 1. The mechanical and fracture parameters are calibrated from experimental data reported in the literature for the same composite system [49, 64], while the electrical parameters are taken from measurements on carbon fibers [65]. The numerical investigations systematically examine the spatial distribution of the crack driving force under viscous relaxation for balanced and unbalanced fiber architectures and the coupled electromechanical response.

The mechanical parameters of the constitutive model were calibrated against experimental force–displacement data reported in [12, 49] for epoxy composites, establishing quantitative agreement for stiffness, peak load, and post-peak softening. For the piezoresistive sub-model, direct experimental validation is beyond the scope of the present work. However, the predicted electromechanical signature is consistent with the experimental observations for CFRP laminates [51, 52].

We first characterize how viscoelastic and viscoplastic energy storage mechanisms differentially contribute to the crack driving force in CF/epoxy composites. Figs. 4 and 5 present polar diagrams of the instantaneous crack driving force  $\mathcal{H}$  at four time instants following an applied uniaxial strain for CF (50 wt%)/epoxy at 296 K. Fig. 4 examines a balanced distribution with equal fiber weight fractions at  $\pm 45^\circ$ , while Fig. 5 presents an unbalanced configuration with 70 wt% at  $-45^\circ$  and 30 wt% at  $+45^\circ$ . The total driving force (black), equilibrium (blue), non-equilibrium (green), and volumetric (red) components are plotted separately to isolate each physical contribution.

For the balanced distribution (Fig. 4), the four-lobed polar pattern reflects the quasi-isotropic symmetry of the  $\pm 45^\circ$  architecture, with maximum energy accumulation along the  $0^\circ$  and  $90^\circ$  directions. As viscous relaxation proceeds from  $t = 10^{-6}$  s (Fig. 4a) to near-equilibrium at  $t = 0.1$  s (Fig. 4d), the total driving force undergoes approximately 40% reduction, driven primarily by the decay of the non-equilibrium (viscous) contribution. The

equilibrium component remains nearly constant throughout, while the volumetric contribution grows monotonically to become the dominant term at later times, reflecting the progressive build-up of tensile hydrostatic stress. For the unbalanced distribution (Fig. 5), the directional bias imposed by the dominant  $-45^\circ$  family breaks the fourfold symmetry, producing an asymmetric pattern in which the lobe aligned with the  $-45^\circ$  fiber direction is noticeably more elongated. Crucially, this directional anisotropy is preserved throughout the entire relaxation history (Figs. 5a–d), demonstrating that fiber architecture fundamentally controls the spatial distribution of the crack driving force irrespective of the viscous state of the matrix.

**Table 1:** Material parameters used in the numerical simulations.

Parameter	Symbol	Value	Equation	References
<i>Viscoelastic-viscoplastic model</i>				
Equilibrium shear modulus	$\mu_{\text{eq}}^0$ (MPa)	760	(28)	[66]
Non-equilibrium shear modulus	$\mu_{\text{neq}}^0$ (MPa)	790	(28)	[66]
Volumetric bulk modulus	$k_v^0$ (MPa)	1154	(37)	[66]
Viscoelastic pre-factor	$\dot{\epsilon}_0$ ( $\text{s}^{-1}$ )	$1.0447 \times 10^{12}$	(12)	[66]
Activation energy	$\Delta H$ (J)	$1.977 \times 10^{-19}$	(12)	[66]
Stress exponent	$m$	0.657	(12)	[66]
Athermal yield stress	$\tau_0$ (MPa)	40	(12)	[66]
Viscoplastic parameter	$a$	$0.22\omega_w + 0.005$	(17)	–
Viscoplastic exponent	$b$	1.1	(17)	–
Viscoplastic threshold	$\sigma_0$ (MPa)	[66]	(17)	–
Temperature sensitivity	$\alpha_\theta$ ( $\text{K}^{-1}$ )	0.01093	(3)	[66]
Fiber stiffness parameter	$a_1$	9	(34)	[3]
Fiber stiffness parameter	$a_2$	1	(34)	[3]
Fiber stiffness parameter	$a_3$	1	(34)	[3]
<i>Phase-field fracture model</i>				
Critical energy release rate	$G_c$ (N/mm)	0.200	(53)	[49]
Length scale parameter	$l_0$ (mm)	0.02	(53)	[49]
<i>Piezoresistive electrical model</i>				
Matrix conductivity	$\sigma_m$ (S/mm)	$10^{-14}$	(91)	–
Axial fiber conductivity	$\sigma_{\parallel}^0$ (S/mm)	66.7	(92)	[65]
Transverse fiber conductivity	$\sigma_{\perp}^0$ (S/mm)	15.9	(93)	[65]
Longitudinal gauge factor	$\text{GF}_{\parallel}$	2.0	(92)	[51]
Transverse gauge factor	$\text{GF}_{\perp}$	2.0	(93)	[51]
Electrical degradation exponent	$p$	2	(97)	–
Residual conductivity	$k_e$	$10^{-6}$	(97)	–
Applied voltage	$V_{\text{app}}$ (V)	1.0	(89)	–

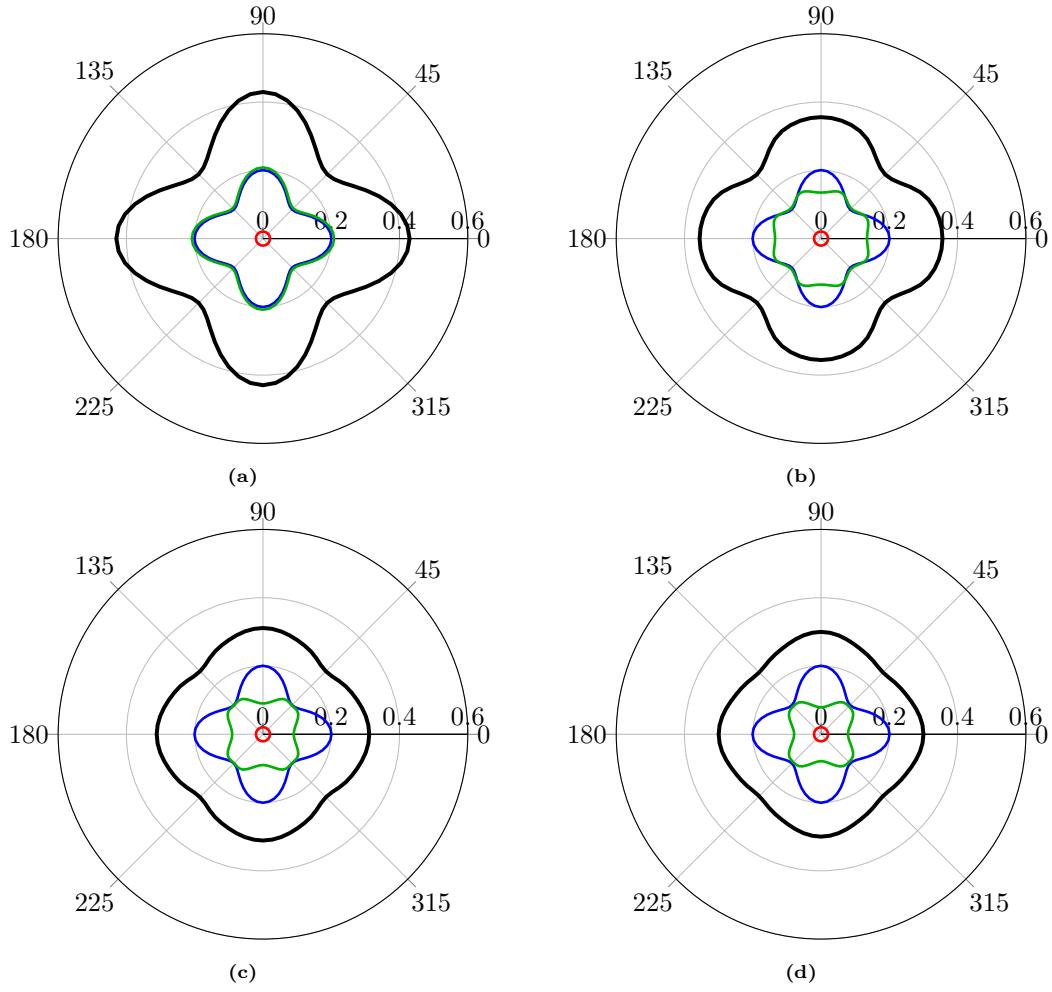


**Figure 4:** Spatial distribution of crack driving force components during viscous relaxation for CF (50 wt%)/epoxy with balanced fiber families oriented at  $\pm 45^\circ$  at 296 K. The contours show (a) initial response at  $t = 10^{-6}$  s, (b) early relaxation at  $t = 0.005$  s, (c) intermediate relaxation at  $t = 0.05$  s, and (d) near-equilibrium at  $t = 0.1$  s. Color coding: total (black), equilibrium (blue), non-equilibrium (green), and volumetric (red) energy contributions.

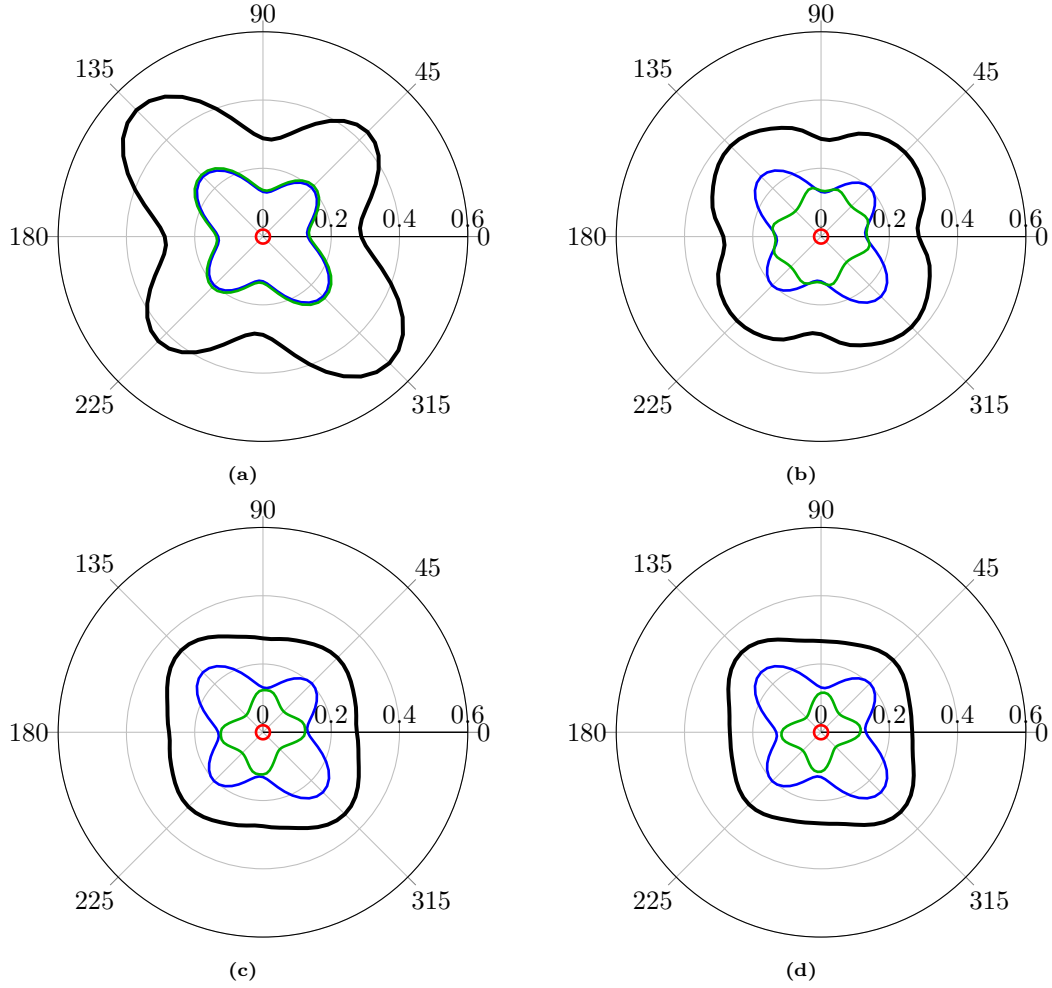


**Figure 5:** Spatial distribution of crack driving force components during viscous relaxation for CF (50 wt%)/epoxy with unbalanced fiber distribution (70 wt% at  $-45^\circ$  and 30 wt% at  $+45^\circ$ ) at 296 K. The contours show (a) initial response at  $t = 10^{-6}$  s, (b) early relaxation at  $t = 0.005$  s, (c) intermediate relaxation at  $t = 0.05$  s, and (d) near-equilibrium at  $t = 0.1$  s. Color coding: total (black), equilibrium (blue), non-equilibrium (green), and volumetric (red) energy contributions.

The temporal evolution of the individual energy contributions for the unbalanced configuration is summarized in Fig. 6. The total driving force  $\mathcal{H}$  rises steeply upon loading and then decays as the non-equilibrium (viscous) energy relaxes, decreasing from its initial peak by approximately 55% at  $t = 0.1$  s. The equilibrium energy reaches a constant value immediately after loading and remains unchanged throughout relaxation, confirming that the equilibrium network stores energy elastically without dissipation. The volumetric energy—initially neg-

ligible—grows monotonically to become the dominant contributor at long times, indicating that the transition from rate-dependent to quasi-elastic fracture behavior is governed by hydrostatic tension build-up. This decomposition confirms a fundamental feature of fracture in viscoelastic-viscoplastic composites: the crack driving force is the sum of time-varying contributions with distinct physical origins, a coupling that cannot be captured by elastic phase-field models.

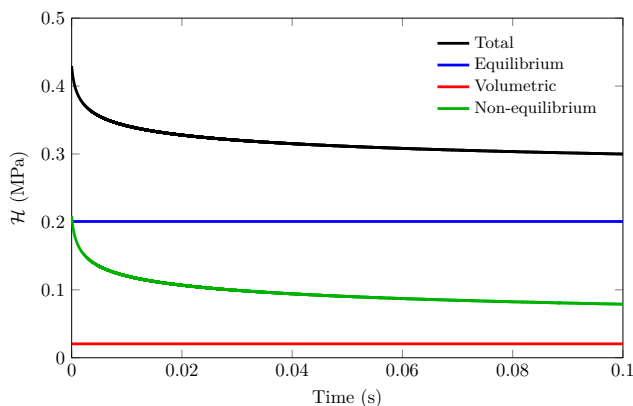


**Figure 6:** Temporal evolution of crack driving force components for CF (50 wt%)/epoxy with unbalanced fiber distribution (70 wt% at  $-45^\circ$  and 30 wt% at  $+45^\circ$ ) at 296 K under uniaxial tensile loading applied at  $45^\circ$  to the horizontal axis.

Figure 7 presents the electromechanical response of CF (30 wt%)/epoxy composites with two  $\pm 45^\circ$  fiber configurations, balanced (50/50) and unbalanced (70/30) weight distributions, at 298 K. The force–displacement curves in Fig. 7a show that both configurations exhibit similar peak loads and initial stiffness, reflecting the equal total fiber content. The slight softening of the 70/30 case arises from the asymmetric crack resistance introduced by the dominant  $-45^\circ$  family, which reduces the effective fracture toughness in the loading direction. The normalized crack length  $\tilde{a}$  in Fig. 7b remains near zero throughout the pre-peak regime and increases sharply at the onset of unstable crack propagation, confirming that crack growth is concentrated in a narrow displacement interval. The 70/30 configuration fractures at a slightly lower displacement than the balanced case, consistent with the reduced resistance offered by the dominant fiber family to crack advance along its preferred direction.

The normalized conductances  $G_{15}/G_{15}^0$  and  $G_{37}/G_{37}^0$  in Figs. 7c–7d decrease monotonically from unity throughout loading, reflecting the progressive degradation of the effective conductivity tensor  $\hat{\sigma}_{\text{eff}}$  driven by the accumulation of  $\phi$ . In the pre-fracture regime both

configurations produce nearly identical conductance trajectories, indicating that the gradual pre-peak damage accumulation is insensitive to the weight ratio asymmetry. The 70/30 configuration produces a steeper conductance drop at an earlier displacement, encoding the earlier fracture displacement directly in the electrical response. Crucially, the two electrode pairs  $G_{15}/G_{15}^0$  and  $G_{37}/G_{37}^0$ , respectively oriented along the main diagonal and horizontally, respond differently to the two configurations. The horizontal pair  $G_{37}/G_{37}^0$  is more sensitive to the asymmetric crack path driven by the dominant  $-45^\circ$  family, while the diagonal pair  $G_{15}/G_{15}^0$  responds more symmetrically. This directional sensitivity, replicated across all 28 electrode pairs, provides the basis for the inverse analysis described in Section 5. Different fiber architectures produce distinguishable conductance signatures, and the multi-electrode network resolves orientation-dependent damage features that a single electrode pair cannot capture.

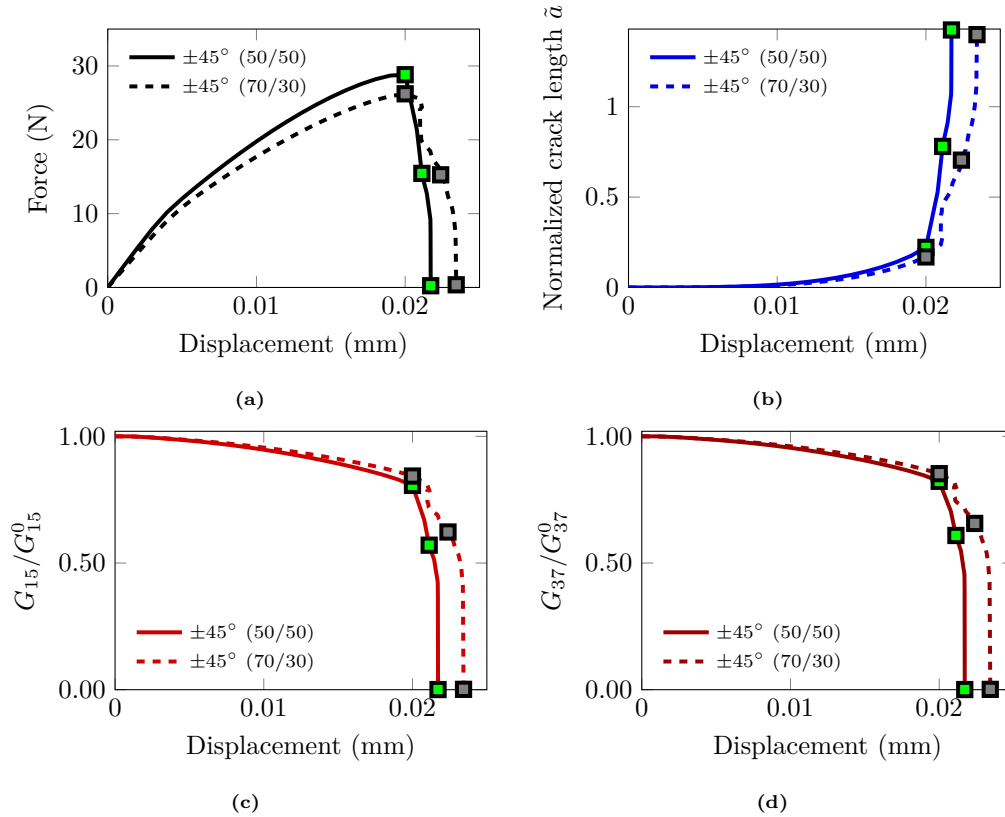


**Figure 7:** Force–displacement response, normalized crack length  $\bar{a}$ , normalized compliance  $\tilde{C}$ , and normalized conductances  $G_{ij}/G_{ij}^0$  vs. applied displacement for CF (30 wt%)/epoxy composite at 298 K.

The spatial evolution of the phase-field variable and electric potential fields at the three marked displacements is shown in Figs. 8 and 9 for the balanced and unbalanced configurations, respectively. In both cases the phase-field contours confirm that crack propagation is confined to a narrow band oriented along the dominant fibre family: the balanced 50/50 configuration produces a nominally horizontal crack path, while the dominant  $-45^\circ$  family in the 70/30 case deflects the crack downward at approximately  $-45^\circ$  to the horizontal. The electric potential fields  $\phi_e$  for the E1→E5 (main diagonal) and E3→E7 (horizontal) pairs respond distinctly to this difference: the horizontal pair is strongly disrupted by the oblique crack in the 70/30 case, producing a more pronounced potential discontinuity across the crack plane, whereas the diagonal pair is comparatively less affected. This orientation-dependent distortion of the potential field is the physical mechanism by which the 28-pair conductance network encodes crack path information, and it motivates the use of the full electrode set as input to the inverse model.

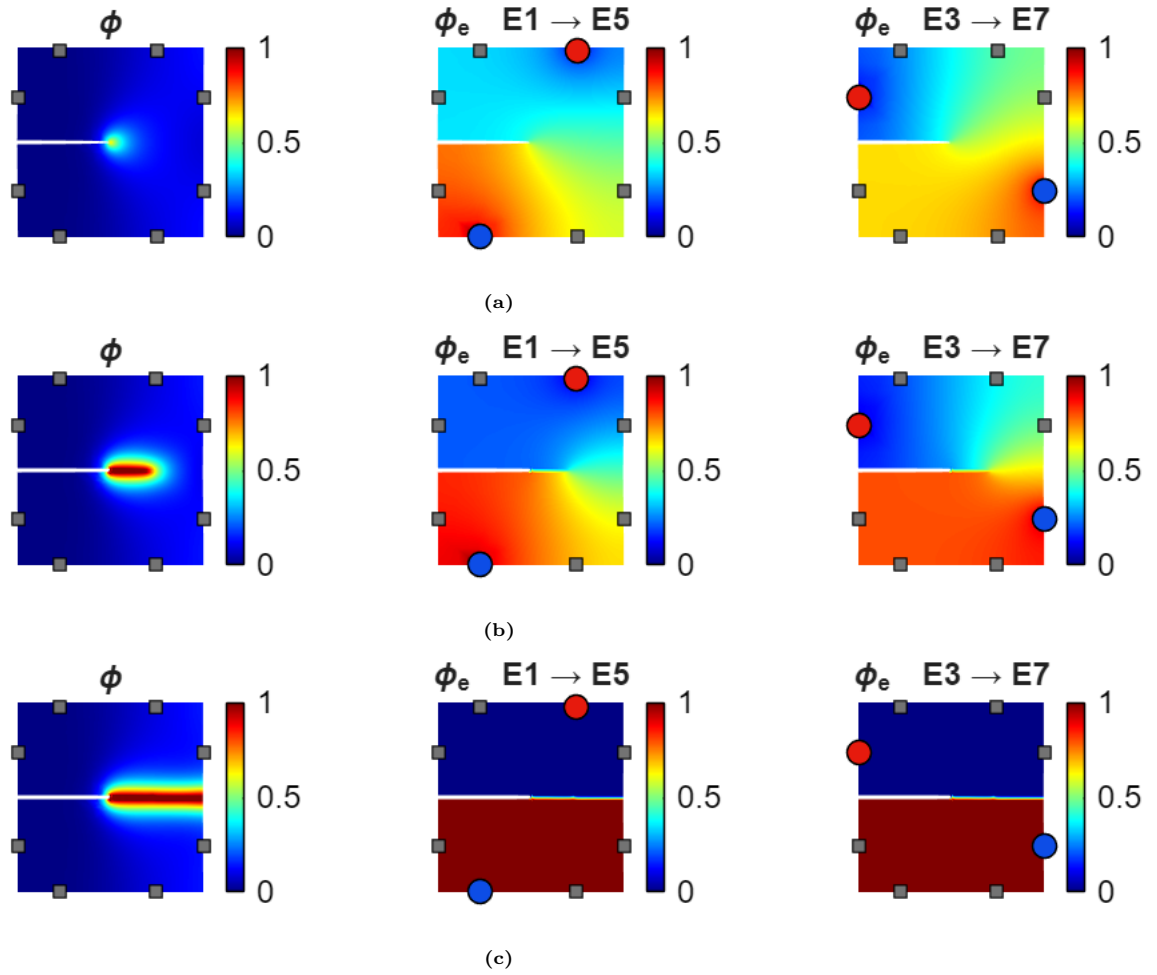


**Figure 8:** Crack propagation in CF (30 wt%)/epoxy composite with  $\pm 45^\circ$  (50/50) fibre configuration at displacements: (a) 0.0200 mm, (b) 0.0211 mm, and (c) 0.0217 mm. The snapshots are marked at the force-displacement response in Fig. 6.

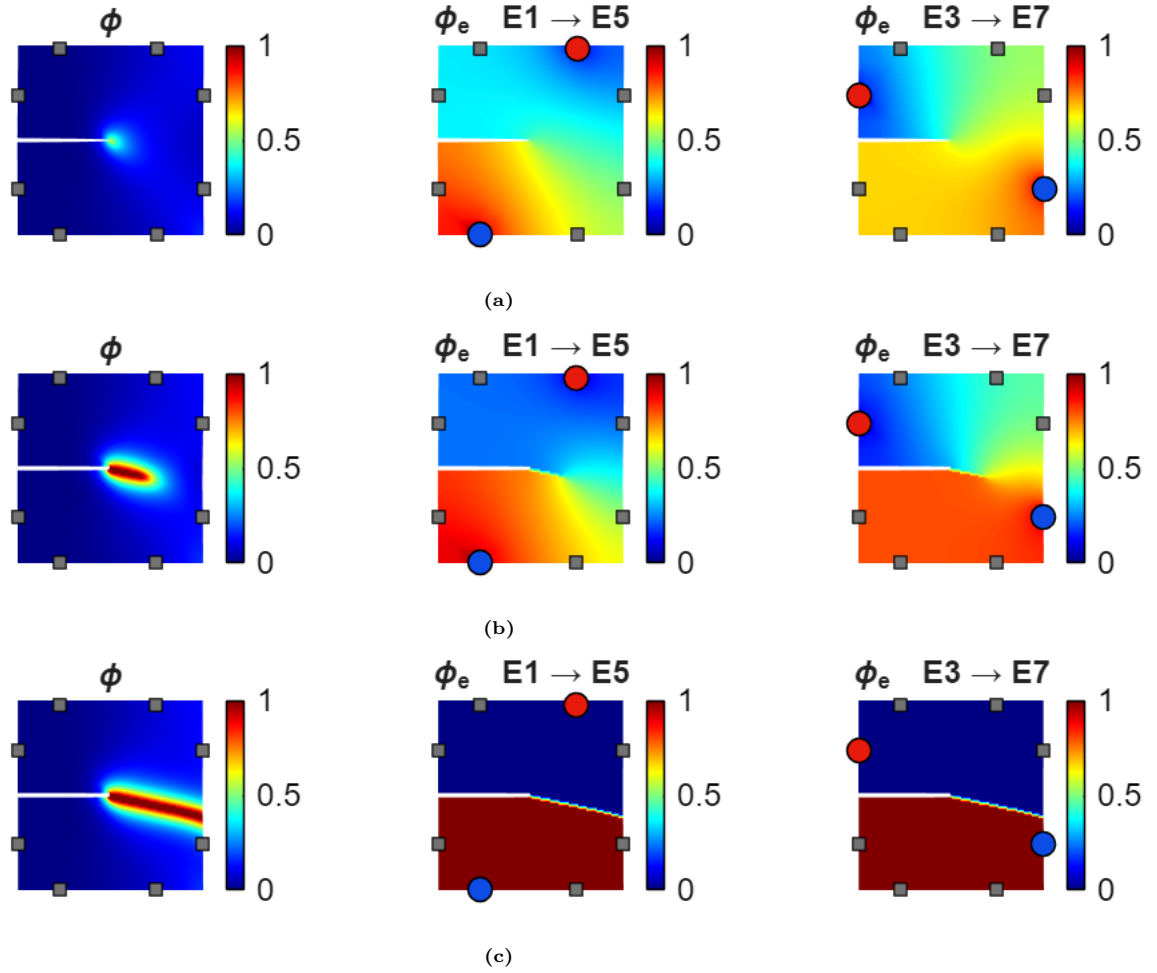
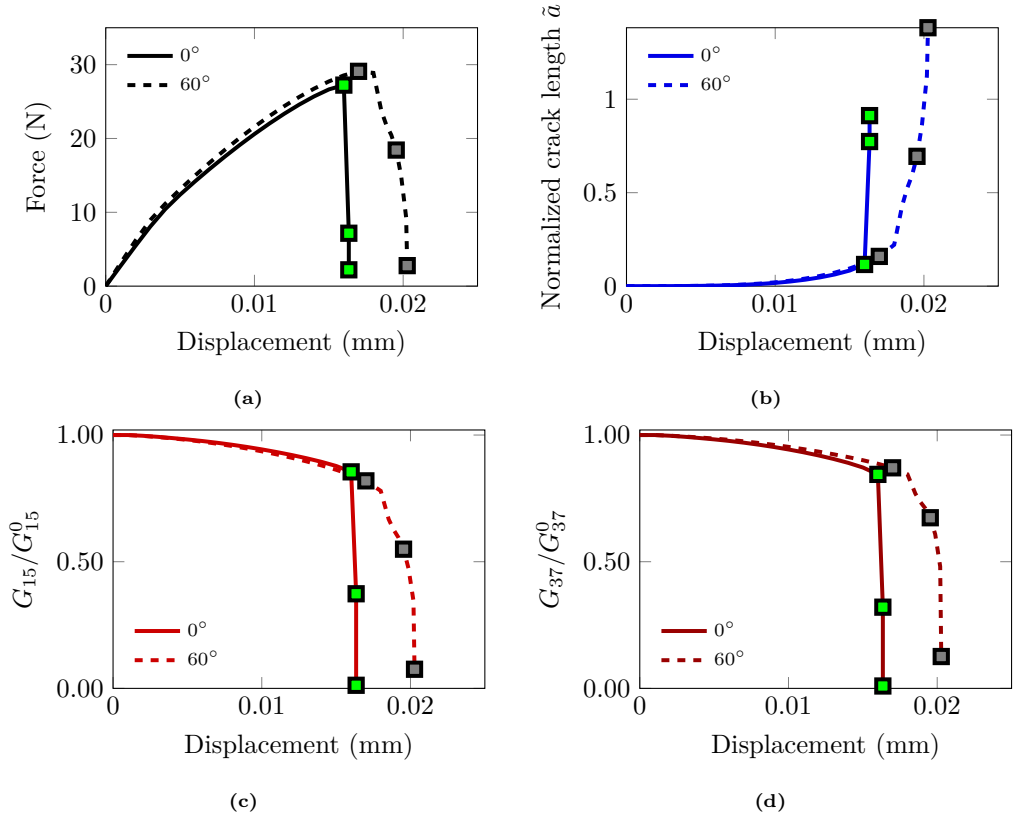


**Figure 9:** Crack propagation in CF (30 wt%)/epoxy composite with  $\pm 45^\circ$  (70/30) fibre configuration at displacements: (a) 0.0200 mm, (b) 0.0224 mm, and (c) 0.0234 mm. The snapshots are marked at the force-displacement response in Fig. 6.

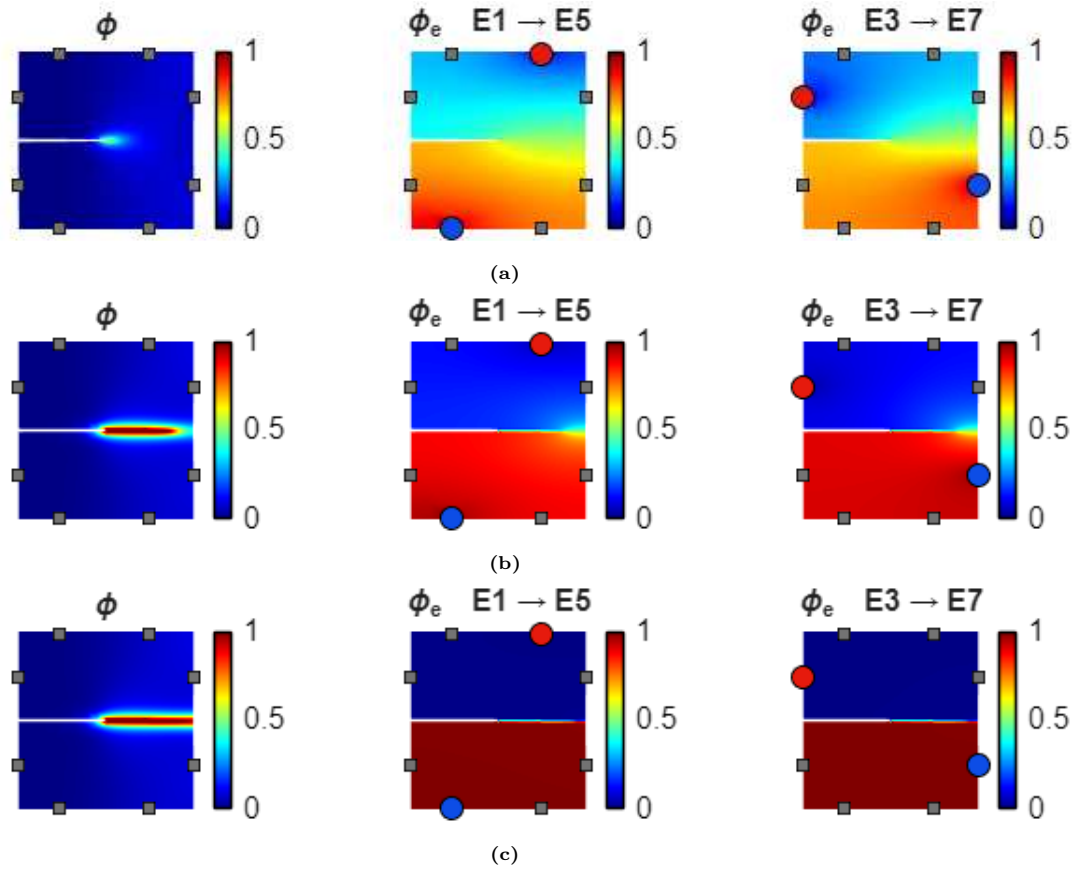
Figure 10 presents the electromechanical response of CF (30 wt%)/epoxy composites with single-fiber-family configurations aligned at  $0^\circ$  and  $60^\circ$  at 298 K. The force-displacement curves in Fig. 10a show that both configurations exhibit similar overall stiffness and peak load, reflecting the identical fiber content and the dominance of the matrix response in the pre-peak regime. The  $0^\circ$  configuration fractures at a slightly lower displacement than the  $60^\circ$  case, as the horizontal fiber alignment offers minimal resistance to mode-I crack opening perpendicular to the loading direction, while the  $60^\circ$  fibers provide a partial deflection mechanism that marginally delays unstable crack propagation.

The normalized crack length  $\tilde{a}$  in Fig. 10(b) exhibits the same characteristic pattern observed in Fig. 7: negligible growth throughout the pre-peak regime followed by a sharp jump at fracture. However, the post-fracture  $\tilde{a}$  values differ between the two configurations, reflecting the different crack path lengths associated with a horizontal crack ( $0^\circ$ ) and an oblique crack ( $60^\circ$ ) traversing the specimen width.

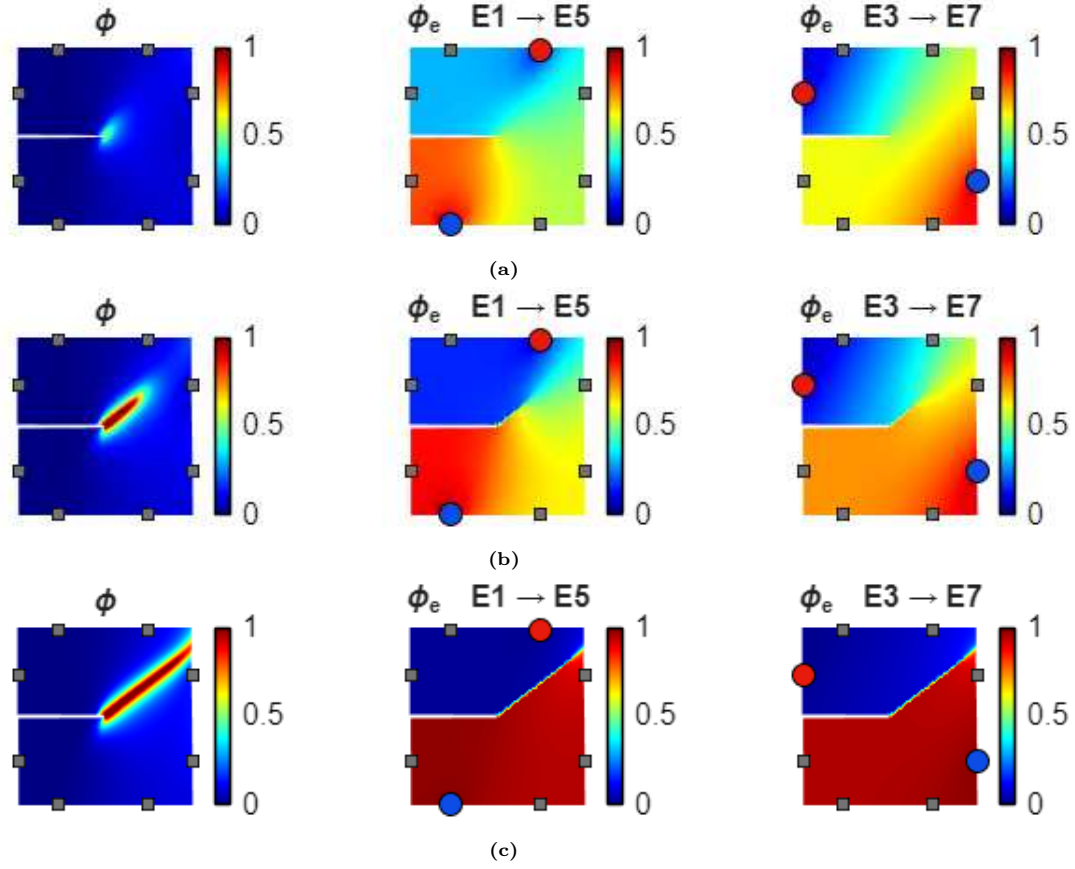
The normalized conductances  $G_{15}/G_{15}^0$  and  $G_{37}/G_{37}^0$  in Figs. 10(c)–(d) reveal a qualitatively different behavior from the  $\pm 45^\circ$  cases. In the pre-fracture regime both configurations again produce similar trajectories, but at fracture the two pairs respond in opposite fashion depending on the crack orientation. For the  $0^\circ$  configuration, the horizontal crack propagates perpendicular to the E1→E5 diagonal pair and parallel to the E3→E7 horizontal pair: the diagonal pair therefore experiences a complete severing of the current path, producing an abrupt and near-total conductance collapse, while the horizontal pair is comparatively less disrupted. For the  $60^\circ$  configuration the crack deflects toward the fiber direction, cutting obliquely across both pairs and producing intermediate conductance drops in both, with the diagonal pair now less affected than in the  $0^\circ$  case. This contrast between the two configurations — barely distinguishable in the force–displacement response but clearly separated in the directional conductance signatures — directly demonstrates the orientation sensitivity of the multi-electrode network and the insufficiency of mechanical measurements alone for fiber architecture identification. The three displacement snapshots marked in Fig. 10 correspond to the phase-field and electric potential contours shown in Figs. 11 and 12, which confirm the distinct spatial crack paths and their contrasting effects on the electric potential distributions for the two electrode pairs shown.



**Figure 10:** Force–displacement response, normalized crack length  $\tilde{a}$ , normalized compliance  $\tilde{C}$ , and normalized conductances  $G_{ij}/G_{ij}^0$  vs. applied displacement for CF (30 wt%)/epoxy composite at 298 K.



**Figure 11:** Crack propagation in CF (30 wt%)/epoxy composite with 0° fibre configuration at displacements: (a) 0.0160 mm, (b) 0.0163 mm, and (c) 0.0164 mm. The snapshots are marked at the force-displacement response in Fig. 9.



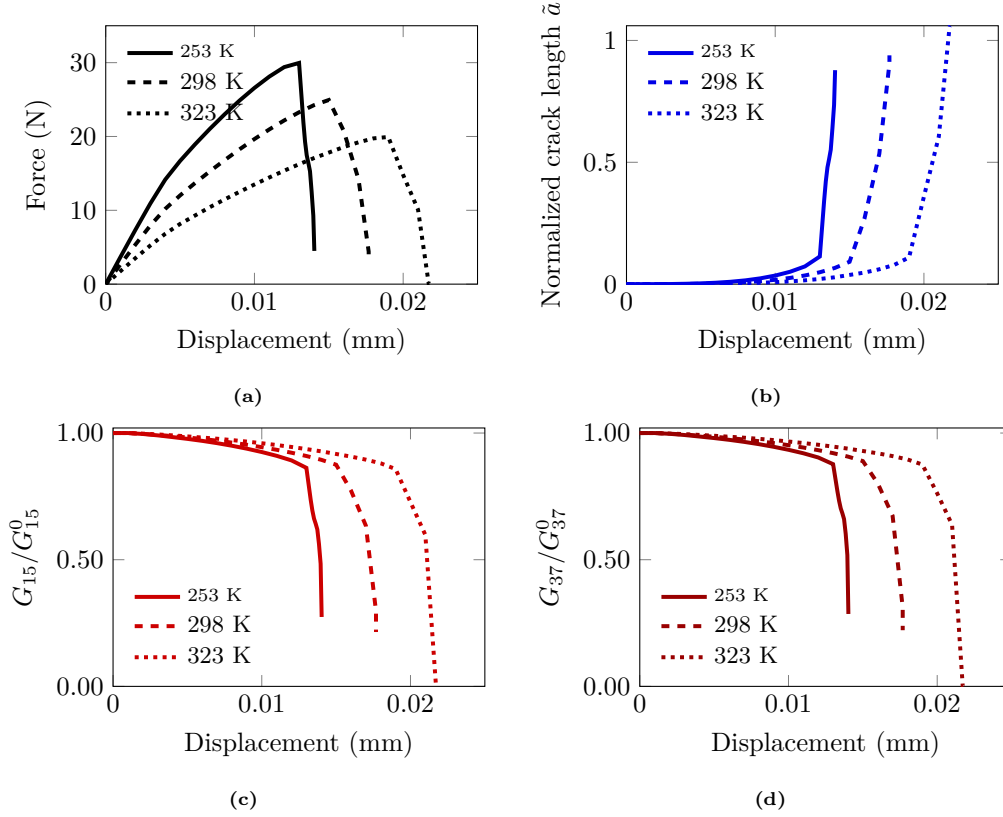
**Figure 12:** Crack propagation in CF (30 wt%)/epoxy composite with  $60^\circ$  fibre configuration at displacements: (a) 0.0200 mm, (b) 0.0224 mm, and (c) 0.0234 mm. The snapshots are marked at the force-displacement response in Fig. 9.

Figure 13 examines the effect of temperature on the electromechanical response of CF (30 wt%)/epoxy composites with randomly oriented fibres at  $v_{CF} = 0.3$ , spanning the temperature range  $\theta \in \{253, 298, 323\}$  K relevant to structural service conditions.

The force-displacement curves in Fig. 13a show a pronounced temperature dependence of both stiffness and peak load: lowering the temperature from 323 K to 253 K increases the peak force from approximately 20 N to 30 N and reduces the fracture displacement, reflecting the stiffening and embrittlement of the epoxy matrix at sub-ambient temperatures governed by the Arrhenius-type viscoelastic flow rule ((12)) and the temperature-sensitive viscoplastic threshold. The normalized crack length  $\bar{a}$  in Fig. 13b exhibits a consistent sharp-onset pattern across all three temperatures, with the fracture displacement shifting to higher

values as temperature increases in accordance with the thermally governed failure displacement identified in the preceding sections.

The normalized conductances  $G_{15}/G_{15}^0$  and  $G_{37}/G_{37}^0$  in Figs. 13c–13d reveal that the pre-fracture conductance trajectories are nearly identical across all three temperatures when plotted against displacement. However, the displacement at which the abrupt conductance drop occurs shifts with temperature. Consequently, when the conductance ratios are mapped against the normalized crack length  $\tilde{a}$  rather than displacement, the three curves collapse onto a single trajectory — confirming that  $\tilde{a}$  is temperature-invariant as a function of the electrical observables. The normalized compliance  $\tilde{C}$ , by contrast, evolves at a different rate with displacement at each temperature because the stiffness degradation rate is governed by the temperature-dependent viscoelastic–viscoplastic material response, and this rate difference is not captured by the conductance ratios alone. This distinction motivates including temperature  $T$  as an explicit input to the inverse model alongside the fiber architecture descriptors and the conductance measurements, as described in Section 6.2.



**Figure 13:** Effect of temperature on the force–displacement response, normalized crack length  $\bar{a}$ , normalized compliance  $\tilde{C}$ , and normalized conductances  $G_{ij}/G_{ij}^0$  vs. applied displacement for CF (30 wt%)/epoxy composite.

## 6.2. Dataset assembly and ANN model training

The training dataset is assembled from a systematic set of phase-field simulations on the single-edge notched specimen described in Section 5, covering a broad range of fiber architectures, carbon fiber contents, and temperatures representative of injection-moulded SCFRP composites in service conditions. All simulations are performed at three temperatures  $T \in \{253, 298, 323\}$  K to capture the effect of thermal loading on the damage-induced piezoresistive response. The simulated configurations are summarised in Table 2. Single-fiber-family cases are generated for eight orientations  $\Theta \in \{-60^\circ, -45^\circ, -30^\circ, 0^\circ, 30^\circ, 45^\circ, 60^\circ, 90^\circ\}$  at  $v_{\text{CF}} = 0.3$ . Two-fiber-family cases with  $\pm 45^\circ$  and  $0^\circ/90^\circ$  are generated for three weight ratios (30/70, 50/50, 70/30), and an additional two-family case covers the  $0^\circ/60^\circ$  (50/50) configuration, all at  $v_{\text{CF}} = 0.3$ . Randomly oriented fibers are simulated at three fiber con-

tents  $v_{\text{CF}} \in \{0.1, 0.3, 0.5\}$ . Two cases are held out entirely from training and used exclusively for validation: the  $0^\circ/60^\circ$  (50/50) two-family configuration at 298 K, and randomly oriented fibers at  $v_{\text{CF}} = 0.3$  across all three temperatures.

**Table 2:** Summary of phase-field simulation cases used for dataset assembly. Test cases are excluded from training.

Fiber architecture	$v_{\text{CF}}$	$\theta$ (K)	Role
Single family, $\Theta = -60^\circ, \dots, 90^\circ$ (8 cases)	0.3	253, 298, 323	Training
Two family, $\pm 45^\circ$ (30/70, 50/50, 70/30)	0.3	253, 298, 323	Training
Two family, $0^\circ/90^\circ$ (30/70, 50/50, 70/30)	0.3	253, 298, 323	Training
Two family, $0^\circ/60^\circ$ (50/50)	0.3	253, 323	Training
Two family, $0^\circ/60^\circ$ (50/50)	0.3	298	<b>Test</b>
Random orientation	0.1, 0.5	253, 298, 323	Training
Random orientation	0.3	253, 323	Training
Random orientation	0.3	298	<b>Test</b>

For each simulation case, post-processing yields one row per saved load step containing the inputs and outputs defined in Eq. (105). Only load steps satisfying  $x_{\text{tip}}/W < 1$  are retained, discarding fully fractured states in which the crack has reached the far boundary and the compliance  $\tilde{C}$  diverges numerically. The initial undamaged state (step 0) is included as a reference row with  $\tilde{a} = 0$ ,  $\tilde{C} = 1$ , and  $G_{ij}^{(0)}/G_{ij}^0 = 1$  for all pairs, providing the model with an explicit representation of the unloaded reference. The assembled training set contains  $N_{\text{train}}$  rows after filtering, and the test set contains  $N_{\text{test}}$  rows from the held-out configuration.

A key design choice is the representation of fiber architecture in the input vector. A scalar fiber angle  $\theta$  is insufficient for two-family configurations with unequal weight ratios: the pairs  $(-45^\circ, 70\%) + (45^\circ, 30\%)$  and  $(-45^\circ, 30\%) + (45^\circ, 70\%)$  are indistinguishable by  $\theta$  alone. The second-order orientation tensor  $\mathbf{A}$  resolves this ambiguity exactly, as it encodes both the principal fiber directions and their relative weights through its eigenvalue decomposition. For the 2D in-plane problem,  $\mathbf{A}$  has two independent components ( $A_{11}$  and  $A_{12}$ , with  $A_{11} + A_{22} = 1$ ), which serve as the microstructure descriptors in the input vector. This parameterisation is consistent with the role of  $\mathbf{A}$  in the forward model, where the same tensor simultaneously defines the anisotropic crack resistance (Section 3) and the principal conduction directions of the carbon fiber network (Section 4). The orientation tensor components for all simulated configurations are listed in Table 3.

It should be noted that several distinct fiber architectures map to the same second-order orientation tensor components. Specifically, the  $\pm 45^\circ$  (50/50),  $0^\circ/90^\circ$  (50/50), and randomly oriented configurations all yield  $(A_{11}, A_{12}) = (0.500, 0.000)$ , and are therefore indistinguishable at the level of  $\mathbf{A}$ . Higher-order orientation tensors would resolve these configurations, but at the cost of a significantly larger input dimension and the need for substantially more training data. Within the present framework this degeneracy is acceptable because the three configurations also produce similar conductance signatures. This degeneracy is acknowledged as a limitation of the second-order tensor parameterisation and motivates future work incorporating higher-order microstructure descriptors.

**Table 3:** Orientation tensor components  $(A_{11}, A_{12})$  for all simulated fiber configurations.

Configuration	$A_{11}$	$A_{12}$
Single family, $-60^\circ$	0.250	-0.433
Single family, $-45^\circ$	0.500	-0.500
Single family, $-30^\circ$	0.750	-0.433
Single family, $0^\circ$	1.000	0.000
Single family, $30^\circ$	0.750	0.433
Single family, $45^\circ$	0.500	0.500
Single family, $60^\circ$	0.250	0.433
Single family, $90^\circ$	0.000	0.000
Two family, $\pm 45^\circ$ (30/70)	0.500	0.200
Two family, $\pm 45^\circ$ (50/50)	0.500	0.000
Two family, $\pm 45^\circ$ (70/30)	0.500	-0.200
Two family, $0^\circ/90^\circ$ (30/70)	0.300	0.000
Two family, $0^\circ/90^\circ$ (50/50)	0.500	0.000
Two family, $0^\circ/90^\circ$ (70/30)	0.700	0.000
Two family, $0^\circ/60^\circ$ (50/50)	0.625	0.217
Random (isotropic)	0.500	0.000

The inverse mapping  $\mathcal{F}$  (Eq. (105)) is approximated by a feedforward ANN with the following structure. The input layer receives the 31-dimensional vector

$$\mathbf{x}^{(n)} = (A_{11}, A_{12}, v_{CF}, G_{12}^{(n)}/G_{12}^0, \dots, G_{78}^{(n)}/G_{78}^0) \in \mathbb{R}^{31}, \quad (106)$$

comprising three microstructure descriptors and 28 normalised conductance ratios for the  $\binom{8}{2} = 28$  electrode pairs. The output layer produces the two-dimensional vector  $\hat{\mathbf{y}}^{(n)} = (\hat{a}^{(n)}, \hat{C}^{(n)}) \in \mathbb{R}^2$ . Two fully connected hidden layers with 16 neurons each and hyperbolic tangent activation functions connect input to output; the output layer uses a linear activation. The total number of trainable parameters is  $(31 \times 16 + 16) + (16 \times 16 + 16) + (16 \times 2 + 2) = 786$ .

All inputs and outputs are z-score normalised prior to training using the mean and standard deviation of the training set exclusively, preventing any leakage of test-set statistics into the model. The network is trained by minimising the mean squared error (MSE) between predicted and true normalised outputs using the Levenberg–Marquardt algorithm [67], which approximates the Hessian of the loss through the Gauss–Newton approximation  $\mathbf{H} \approx \mathbf{J}^T \mathbf{J}$  and is well-suited for small-to-medium regression networks where the full Jacobian can be formed. Training is terminated by early stopping with a patience of 20 epochs, monitoring the MSE on a 15% validation split drawn randomly from the training set. The maximum number of training epochs is set to 1000. Convergence is consistently achieved before this limit.

The training history of the ANN model is shown in Fig. 14. Both the training and validation MSE decrease rapidly during the first 20 epochs, reflecting the fast convergence characteristic of the Levenberg–Marquardt algorithm in the early phase of training where the loss surface is far from any local minimum. Beyond epoch 20 the training MSE continues to decrease steadily, reaching approximately  $10^{-6}$  at the final epoch, while the validation MSE plateaus at around  $10^{-4}$  and remains stable throughout the remainder of training. The gap between the two curves is moderate and does not widen with continued training, confirming the absence of overfitting despite the relatively small network size of 786 trainable parameters. Early stopping terminates training at epoch 116, identified as the best validation epoch, at which point the model weights are frozen and used for all subsequent predictions. The smooth monotonic decrease of both loss curves, with no instabilities or oscillations, confirms that the Levenberg–Marquardt optimizer converges reliably for the present regression task and that the 15% validation split provides a stable early stopping signal throughout training.

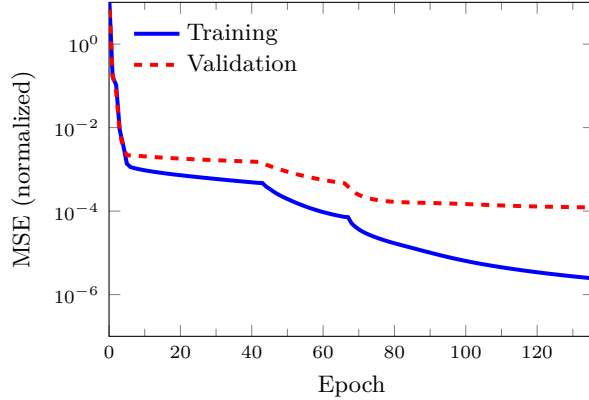


**Figure 14:** Training history of the ANN model. Training and validation MSE (normalized) vs. epoch. The dotted vertical line marks the best validation epoch (epoch 116).

The predictive accuracy of the trained ANN model is assessed through parity plots for the training, validation, and test sets, shown in Fig. 15. In all six panels the predicted values lie close to the identity line, confirming that the model learns the underlying input–output mapping rather than memorizing the training data.

For the normalized crack length  $\tilde{a}$  (Figs. 15a–c), the training and validation sets show near-perfect agreement between predicted and true values across the full range  $\tilde{a} \in [0, 0.25]$ . The test set, comprising the held-out  $0^\circ/60^\circ$  (50/50) two-family configuration at 298 K – a fiber architecture not present in any training case – yields  $R^2 = 0.995$  and root mean square error (RMSE) =  $5.7 \times 10^{-3}$ . This result demonstrates that the orientation tensor parameterization  $(A_{11}, A_{12})$  provides sufficient microstructure information for the model to generalize to an unseen fiber configuration, interpolating smoothly between the single-family and two-family training cases.

For the normalized compliance  $\tilde{C}$  (Figs. 15d–f), the training and validation predictions are again tightly clustered along the identity line across the range  $\tilde{C} \in [1, 2]$ . The test set yields  $R^2 = 1.000$  and RMSE =  $5.7 \times 10^{-3}$ , indicating that the compliance trajectory of the held-out configuration is predicted with virtually no systematic error. The consistent performance across training, validation, and test splits confirms that the model generalizes well and that the 15% validation split used for early stopping provides a representative assessment of out-of-sample accuracy. Taken together, the parity plots establish that a compact feedforward network with only 786 trainable parameters and a 31-dimensional input is sufficient to approximate the nonlinear inverse mapping  $\mathcal{F}$  (Eq. (105)) with high fidelity across the full range of fiber architectures, fiber contents, and damage states represented in the dataset.

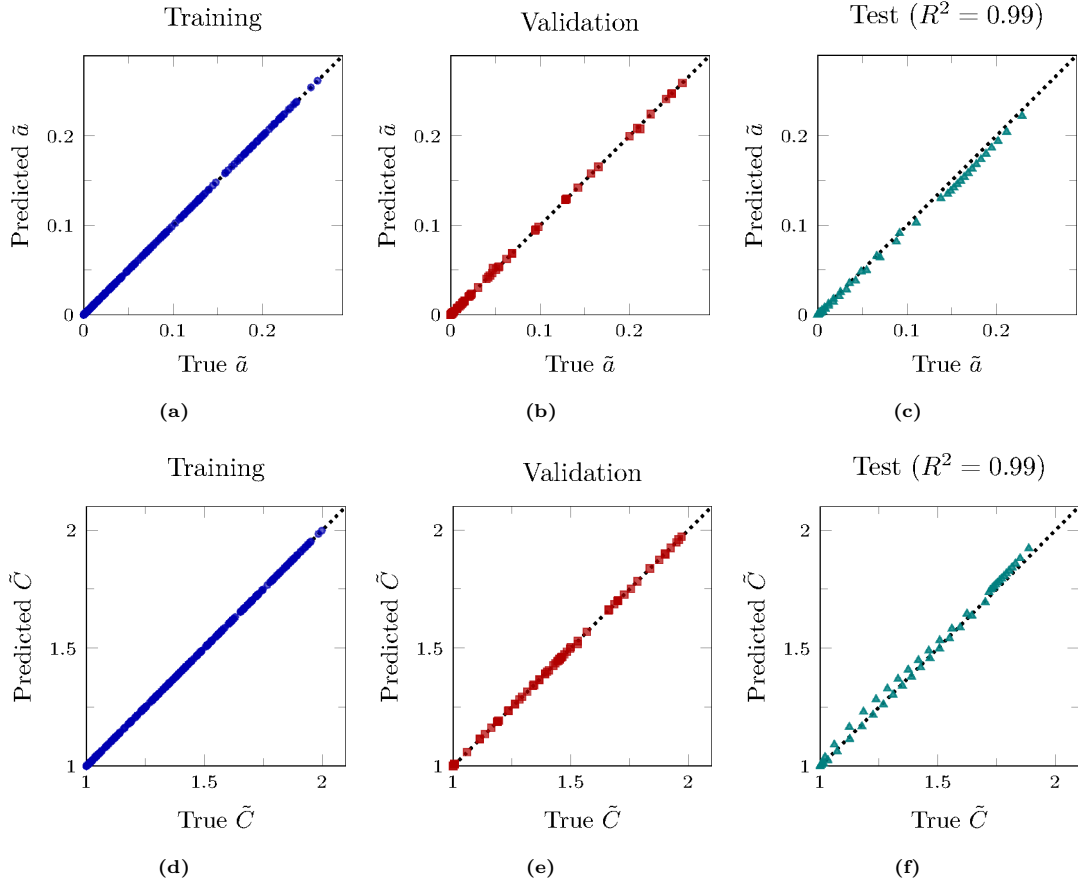


**Figure 15:** Parity plots for the ANN model. Top row: normalized crack length  $\tilde{a}$ . Bottom row: normalized compliance  $\tilde{C}$ . Columns correspond to the training, validation, and test (held-out  $0^\circ/60^\circ$  50/50) sets. Dotted lines indicate perfect agreement.

Fig. 16 demonstrates the SHM capability of the proposed inverse framework for a held-out test case consisting of randomly oriented fibers with a carbon fiber content of  $\nu_{CF} = 0.3$  at 298 K. The figure compares the ground-truth phase-field simulation data with the predictions of the trained ANN for two global damage indicators: the normalized crack length  $\tilde{a}$  and the normalized compliance  $\tilde{C}$ . In Fig. 16a, the ANN accurately reproduces the evolution of the normalized crack length throughout the loading history, including both the gradual pre-fracture regime and the abrupt increase associated with unstable crack propagation. The predicted trajectory remains nearly indistinguishable from the true phase-field response, confirming that the conductance-based electrical measurements contain sufficient information to infer the progression of fracture in randomly oriented fiber architectures that were excluded

from training. Fig. 16b presents the corresponding prediction of the normalized compliance  $\tilde{C}$ , where the ANN again captures the stiffness degradation response with excellent agreement over all load steps. The close overlap between the predicted and reference curves demonstrates that the inverse model successfully reconstructs both fracture evolution and structural softening directly from the multi-electrode conductance measurements. Since the randomly oriented configuration represents a microstructure with diffuse anisotropy rather than a dominant fiber direction, the results confirm the robustness of the orientation-tensor parameterization and the ability of the ANN to generalize to isotropic-like architectures not explicitly included in the training dataset.

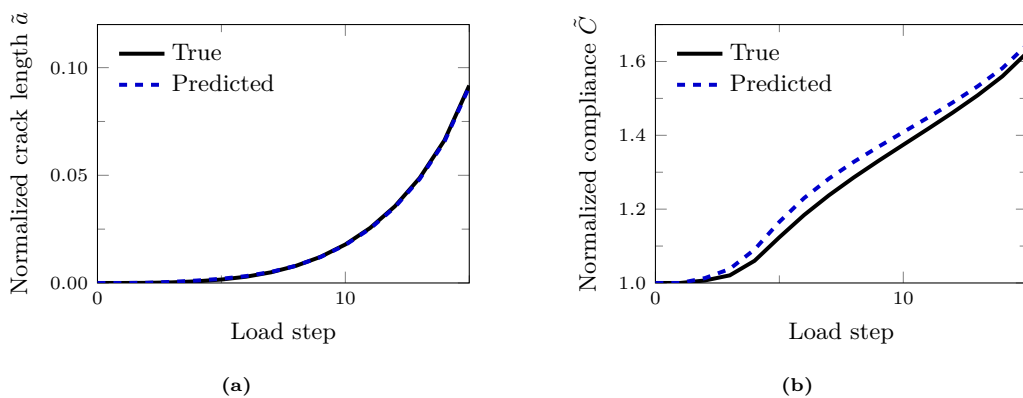


**Figure 16:** SHM scenario demonstration for the held-out test case (randomly oriented fibers,  $v_{CF} = 0.3$ ) at 298 K. True phase-field values (solid black) and ANN predictions (dashed blue) of (a) normalized crack length  $\tilde{a}$  and (b) normalized compliance  $\tilde{C}$  vs. load step.

Fig. 17 presents a second SHM demonstration for the held-out two-family fiber configuration consisting of  $0^\circ/60^\circ$  fibers with a balanced (50/50) weight distribution at  $v_{CF} = 0.3$  and 298 K. This configuration was intentionally excluded from the ANN training dataset in order to evaluate the model’s capability to interpolate between previously observed fiber architectures. Fig. 17a compares the true and predicted normalized crack length  $\tilde{a}$  as a function of load step. The ANN accurately captures both the onset and progression of crack growth, including the sharp increase associated with unstable fracture propagation. The prediction closely follows the phase-field reference solution across the entire loading history, demonstrating that the orientation tensor representation provides sufficient information for the inverse model to reconstruct damage evolution in previously unseen anisotropic fiber configurations. Fig. 17b shows the corresponding prediction of the normalized compliance  $\tilde{C}$ . The ANN

reproduces the stiffness degradation trajectory with negligible deviation from the reference solution, accurately capturing the nonlinear compliance increase accompanying progressive damage accumulation. The excellent agreement observed in both panels confirms that the proposed inverse framework generalizes effectively beyond the training set and can reliably infer the internal damage state of composites with arbitrary fiber architectures directly from electrical conductance measurements. These results demonstrate the feasibility of combining the multiphysics phase-field simulations with machine-learning-based inversion for real-time structural health monitoring of short carbon fiber-reinforced polymer composites.

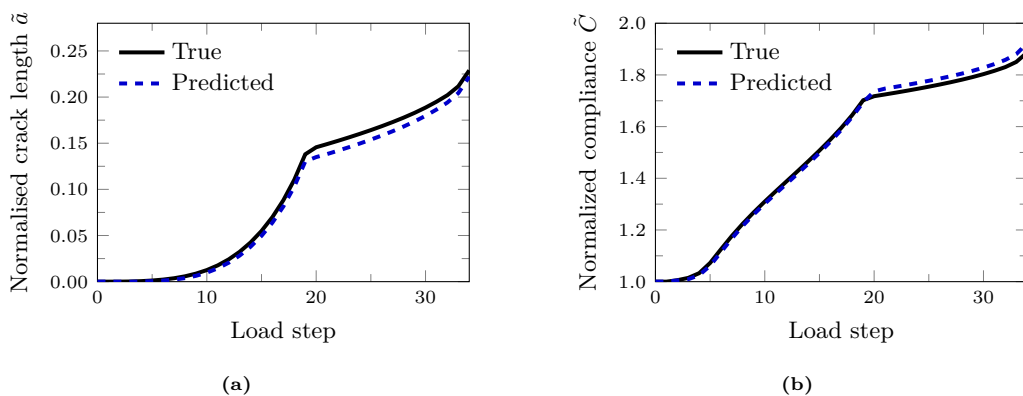


**Figure 17:** SHM scenario demonstration for the held-out test case ( $0^\circ/60^\circ$  50/50 fiber configuration,  $v_{CF} = 0.3$ ) at 298 K. True phase-field values (solid black) and ANN predictions (dashed blue) of (a) normalized crack length  $\tilde{a}$  and (b) normalized compliance  $\tilde{C}$  vs. load step.

## 7. Summary and conclusions

This work presented a multiphysics phase-field framework for modeling anisotropic viscoelastic-viscoplastic fracture and damage-induced piezoresistive response in SCFRP composites at finite deformation. The second-order fiber orientation tensor  $\mathbf{A}$  serves as the common thread connecting three coupled sub-problems (i.e., the viscoelastic-viscoplastic constitutive model, the anisotropic phase-field fracture formulation, and the piezoresistive conductivity model) by simultaneously defining the principal fiber family directions, the anisotropic crack resistance, and the principal conduction paths of the carbon fiber network. The coupled framework is combined with an EIT configuration and a feedforward ANN for real-time inverse damage identification from conductance measurements alone. The key findings are as follows.

- The normalized conductivity  $\sigma/\sigma_0$  remains near unity throughout pre-peak loading and

drops abruptly at fracture onset, coinciding with irreversible severance of conductive fiber pathways. The spatial conductivity field encodes the crack trajectory, providing orientation-sensitive damage information beyond what force–displacement measurements alone can offer.

- Fiber orientation governs both crack path morphology and conductivity evolution. Different fiber architectures produce distinguishable conductance signatures across all 28 electrode pairs, providing the physical basis for orientation-sensitive inverse damage analysis.
- Increasing carbon fiber content from 10 to 50 wt% progressively enhances stiffness, peak load, and fracture energy. Randomly oriented fibers yield a horizontal mode-I crack and a straight conductivity boundary, in contrast to the inclined boundaries imposed by aligned configurations.
- The trained ANN achieves  $R^2 = 0.99$  on held-out fiber configurations absent from training, confirming that the orientation tensor parameterization enables generalization across the microstructure space and that real-time data-driven structural health monitoring of SCFRP composites is feasible.

Future work should address the degeneracy of the second-order orientation tensor for configurations sharing identical  $(A_{11}, A_{12})$  values through higher-order microstructure descriptors, extend the piezoresistive model to account for fiber–matrix interface debonding at the micromechanical level, and generalize the framework to fatigue damage under cyclic electromechanical loading and to dynamic fracture under impact conditions.

## Acknowledgements

The authors acknowledge the resources and support provided by the Norwegian Research Infrastructure Services (NRIS). The computational work was performed on resources provided through the Sigma2 national e-infrastructure, project NN10041K.

## References

- [1] J. Holbery, D. Houston, Natural-fiber-reinforced polymer composites in automotive applications, *Jom* 58 (11) (2006) 80–86.

- [2] C. Soutis, Carbon fiber reinforced plastics in aircraft construction, *Materials Science and Engineering: A* 412 (1-2) (2005) 171–176.
- [3] B. Arash, W. Exner, R. Rolfes, Viscoelastic damage behavior of fiber reinforced nanoparticle-filled epoxy nanocomposites: Multiscale modeling and experimental validation, *Composites Part B: Engineering* 174 (2019) 107005.
- [4] D. Chung, Continuous carbon fiber polymer-matrix composites and their joints, studied by electrical measurements, *Polymer Composites* 22 (2) (2001) 250–270.
- [5] S. Wang, D. Chung, Self-sensing of flexural strain and damage in carbon fiber polymer-matrix composite by electrical resistance measurement, *Carbon* 44 (13) (2006) 2739–2751.
- [6] A. A. Gusev, Finite element estimates of viscoelastic stiffness of short glass fiber reinforced composites, *Composite Structures* 171 (2017) 53–62.
- [7] Z. Wang, D. E. Smith, Numerical analysis on viscoelastic creep responses of aligned short fiber reinforced composites, *Composite Structures* 229 (2019) 111394.
- [8] X. Poulain, A. Benzerga, R. Goldberg, Finite-strain elasto-viscoplastic behavior of an epoxy resin: Experiments and modeling in the glassy regime, *International Journal of Plasticity* 62 (2014) 138–161.
- [9] B. Arash, R. Unger, W. Exner, R. Rolfes, A finite deformation gradient-enhanced damage model for nanoparticle/polymer nanocomposites: An atomistically-informed multiscale approach, *Composite Structures* 258 (2021) 113211.
- [10] B. Arash, S. Zakavati, B. Bahtiri, M. Jux, R. Rolfes, Phase-field modeling of fracture in viscoelastic–viscoplastic thermoset nanocomposites under cyclic and monolithic loading, *Engineering with Computers* 41 (1) (2025) 681–701.
- [11] Y. Zhou, F. Pervin, L. Lewis, S. Jeelani, Experimental study on the thermal and mechanical properties of multi-walled carbon nanotube-reinforced epoxy, *Materials Science and Engineering: A* 452 (2007) 657–664.
- [12] B. Bahtiri, B. Arash, S. Scheffler, M. Jux, R. Rolfes, A machine learning-based viscoelastic–viscoplastic model for epoxy nanocomposites with moisture content, *Computer Methods in Applied Mechanics and Engineering* 415 (2023) 116293.

- [13] M. Ortiz, A. Pandolfi, Finite-deformation irreversible cohesive elements for three-dimensional crack-propagation analysis, *International journal for numerical methods in engineering* 44 (9) (1999) 1267–1282.
- [14] S. Li, M. Thouless, A. Waas, J. Schroeder, P. Zavattieri, Use of a cohesive-zone model to analyze the fracture of a fiber-reinforced polymer–matrix composite, *Composites science and technology* 65 (3-4) (2005) 537–549.
- [15] I. Lapczyk, J. A. Hurtado, Progressive damage modeling in fiber-reinforced materials, *Composites Part A: Applied science and manufacturing* 38 (11) (2007) 2333–2341.
- [16] M. G. Pike, C. Oskay, Xfem modeling of short microfiber reinforced composites with cohesive interfaces, *Finite Elements in Analysis and Design* 106 (2015) 16–31.
- [17] M. Kästner, S. Müller, F. Hirsch, J.-S. Pap, I. Jansen, V. Ulbricht, Xfem modeling of interface failure in adhesively bonded fiber-reinforced polymers, *Advanced Engineering Materials* 18 (3) (2016) 417–426.
- [18] G. A. Francfort, J.-J. Marigo, Revisiting brittle fracture as an energy minimization problem, *Journal of the Mechanics and Physics of Solids* 46 (8) (1998) 1319–1342.
- [19] B. Bourdin, G. A. Francfort, J.-J. Marigo, Numerical experiments in revisited brittle fracture, *Journal of the Mechanics and Physics of Solids* 48 (4) (2000) 797–826.
- [20] C. Miehe, M. Hofacker, F. Welschinger, A phase field model for rate-independent crack propagation: Robust algorithmic implementation based on operator splits, *Computer Methods in Applied Mechanics and Engineering* 199 (45-48) (2010) 2765–2778.
- [21] M. Ambati, T. Gerasimov, L. De Lorenzis, A review on phase-field models of brittle fracture and a new fast hybrid formulation, *Computational Mechanics* 55 (2) (2015) 383–405.
- [22] J.-Y. Wu, V. P. Nguyen, C. T. Nguyen, D. Sutula, S. Sinaie, S. P. Bordas, Phase-field modeling of fracture, *Advances in applied mechanics* 53 (2020) 1–183.
- [23] C. Miehe, F. Welschinger, M. Hofacker, Thermodynamically consistent phase-field models of fracture: Variational principles and multi-field fe implementations, *International journal for numerical methods in engineering* 83 (10) (2010) 1273–1311.

- [24] M. J. Borden, C. V. Verhoosel, M. A. Scott, T. J. Hughes, C. M. Landis, A phase-field description of dynamic brittle fracture, *Computer Methods in Applied Mechanics and Engineering* 217 (2012) 77–95.
- [25] M. Ambati, T. Gerasimov, L. De Lorenzis, Phase-field modeling of ductile fracture, *Computational Mechanics* 55 (2015) 1017–1040.
- [26] C. Miehe, S. Mauthe, Phase field modeling of fracture in multi-physics problems. part iii. crack driving forces in hydro-poro-elasticity and hydraulic fracturing of fluid-saturated porous media, *Computer Methods in Applied Mechanics and Engineering* 304 (2016) 619–655.
- [27] A. Dean, J. Mavani, B. Bahtiri, B. Arash, R. Rolfes, A hybrid electromechanical phase-field and deep learning framework for predicting fracture in dielectric nanocomposites, *Engineering Fracture Mechanics* (2026) 111906.
- [28] C. V. Verhoosel, R. De Borst, A phase-field model for cohesive fracture, *International Journal for numerical methods in Engineering* 96 (1) (2013) 43–62.
- [29] B. Li, C. Peco, D. Millán, I. Arias, M. Arroyo, Phase-field modeling and simulation of fracture in brittle materials with strongly anisotropic surface energy, *International Journal for Numerical Methods in Engineering* 102 (3-4) (2015) 711–727.
- [30] S. Teichtmeister, D. Kienle, F. Aldakheel, M.-A. Keip, Phase field modeling of fracture in anisotropic brittle solids, *International Journal of Non-Linear Mechanics* 97 (2017) 1–21.
- [31] J. Clayton, J. Knap, Phase field modeling of directional fracture in anisotropic polycrystals, *Computational Materials Science* 98 (2015) 158–169.
- [32] M. Hofacker, C. Miehe, A phase field model of dynamic fracture: Robust field updates for the analysis of complex crack patterns, *International Journal for Numerical Methods in Engineering* 93 (3) (2013) 276–301.
- [33] Z. A. Wilson, M. J. Borden, C. M. Landis, A phase-field model for fracture in piezoelectric ceramics, *International Journal of Fracture* 183 (2) (2013) 135–153.
- [34] C. Miehe, L.-M. Schaezel, H. Ulmer, Phase field modeling of fracture in multi-physics problems. part i. balance of crack surface and failure criteria for brittle crack propagation

- in thermo-elastic solids, *Computer Methods in Applied Mechanics and Engineering* 294 (2015) 449–485.
- [35] J. Bleyer, R. Alessi, Phase-field modeling of anisotropic brittle fracture including several damage mechanisms, *Computer Methods in Applied Mechanics and Engineering* 336 (2018) 213–236.
- [36] O. Gültekin, H. Dal, G. A. Holzapfel, A phase-field approach to model fracture of arterial walls: theory and finite element analysis, *Computer methods in applied mechanics and engineering* 312 (2016) 542–566.
- [37] A. Dean, P. A. V. Kumar, J. Reinoso, C. Gerendt, M. Paggi, E. Mahdi, R. Rolfes, A multi phase-field fracture model for long fiber reinforced composites based on the puck theory of failure, *Composite Structures* (2020) 112446.
- [38] S. Lv, J. Hua, Y. Shi, C.-F. Gao, An anisotropic phase-field framework for finite-deformation fracture and fatigue in flexible piezoelectric composites, *Engineering Fracture Mechanics* (2026) 111960.
- [39] A. Dean, J. Reinoso, N. Jha, E. Mahdi, R. Rolfes, A phase field approach for ductile fracture of short fibre reinforced composites, *Theoretical and Applied Fracture Mechanics* 106 (2020) 102495.
- [40] K. Au-Yeung, A. Quintanas-Corominas, E. Martínez-Pañeda, W. Tan, Hygroscopic phase field fracture modelling of composite materials, *Engineering with Computers* 39 (6) (2023) 3847–3864.
- [41] F. P. Duda, A. Ciarbonetti, P. J. Sánchez, A. E. Huespe, A phase-field/gradient damage model for brittle fracture in elastic–plastic solids, *International Journal of Plasticity* 65 (2015) 269–296.
- [42] J. Ulloa, P. Rodríguez, C. Samaniego, E. Samaniego, Phase-field modeling of fracture for quasi-brittle materials, *Underground Space* 4 (1) (2019) 10–21.
- [43] F. Dammaß, K. A. Kalina, M. Ambati, M. Käßtner, Phase-field modelling and analysis of rate-dependent fracture phenomena at finite deformation, *Computational Mechanics* (2023) 1–25.

- [44] P. K. A. V. Kumar, A. Dean, J. Reinoso, M. Paggi, Nonlinear thermo-elastic phase-field fracture of thin-walled structures relying on solid shell concepts, *Computer Methods in Applied Mechanics and Engineering* 396 (2022) 115096.
- [45] B. Yin, J. Storm, M. Kaliske, Viscoelastic phase-field fracture using the framework of representative crack elements, *International Journal of Fracture* 237 (1-2) (2022) 139–163.
- [46] R. Shen, H. Waisman, L. Guo, Fracture of viscoelastic solids modeled with a modified phase field method, *Computer Methods in Applied Mechanics and Engineering* 346 (2019) 862–890.
- [47] P. J. Loew, B. Peters, L. A. Beex, Rate-dependent phase-field damage modeling of rubber and its experimental parameter identification, *Journal of the Mechanics and Physics of Solids* 127 (2019) 266–294.
- [48] R. Brighenti, T. Rabczuk, X. Zhuang, Phase field approach for simulating failure of viscoelastic elastomers, *European Journal of Mechanics-A/Solids* 85 (2021) 104092.
- [49] B. Arash, W. Exner, R. Rolfes, Effect of moisture on the nonlinear viscoelastic fracture behavior of polymer nanocomposites: a finite deformation phase-field model, *Engineering with Computers* 39 (1) (2023) 773–790.
- [50] B. Arash, S. Zakavati, T. Rabczuk, A phase-field framework for anisotropic viscoelastic-viscoplastic fracture in short fiber-reinforced polymers in hygrothermal environments, *Engineering Fracture Mechanics* (2026) 112219.
- [51] J. Abry, S. Bochart, A. Chateauminois, M. Salvia, G. Giraud, In situ detection of damage in cfrp laminates by electrical resistance measurements, *Composites science and technology* 59 (6) (1999) 925–935.
- [52] A. Todoroki, J. Yoshida, Electrical resistance change of unidirectional cfrp due to applied load, *JSME International Journal Series A Solid Mechanics and Material Engineering* 47 (3) (2004) 357–364.
- [53] G. J. Gallo, E. T. Thostenson, Electrical characterization and modeling of carbon nanotube and carbon fiber self-sensing composites for enhanced sensing of microcracks, *Materials today communications* 3 (2015) 17–26.

- [54] S. Govindjee, S. Reese, A presentation and comparison of two large deformation viscoelasticity models, *Journal of engineering materials and technology* 119 (3) (1997) 251–255.
- [55] H. Qi, M. Boyce, Stress–strain behavior of thermoplastic polyurethanes, *Mechanics of Materials* 37 (8) (2005) 817–839.
- [56] M. C. Boyce, D. M. Parks, A. S. Argon, Large inelastic deformation of glassy polymers. part i: rate dependent constitutive model, *Mechanics of Materials* 7 (1) (1988) 15–33.
- [57] E. M. Arruda, M. C. Boyce, A three-dimensional constitutive model for the large stretch behavior of rubber elastic materials, *Journal of the Mechanics and Physics of Solids* 41 (2) (1993) 389–412.
- [58] J. C. Simo, Algorithms for static and dynamic multiplicative plasticity that preserve the classical return mapping schemes of the infinitesimal theory, *Computer Methods in Applied Mechanics and Engineering* 99 (1) (1992) 61–112.
- [59] S. Reese, S. Govindjee, A theory of finite viscoelasticity and numerical aspects, *International journal of solids and structures* 35 (26-27) (1998) 3455–3482.
- [60] M. Ambati, R. Kruse, L. De Lorenzis, A phase-field model for ductile fracture at finite strains and its experimental verification, *Computational Mechanics* 57 (1) (2016) 149–167.
- [61] R. Unger, B. Arash, W. Exner, R. Rolfes, Effect of temperature on the viscoelastic damage behaviour of nanoparticle/epoxy nanocomposites: Constitutive modelling and experimental validation, *Polymer* 191 (2020) 122265.
- [62] W. Sun, E. L. Chaikof, M. E. Levenston, Numerical approximation of tangent moduli for finite element implementations of nonlinear hyperelastic material models, *Journal of biomechanical engineering* 130 (6) (2008).
- [63] A. Todoroki, J. Yoshida, Apparent negative piezoresistivity of single-ply cfrp due to poor electrical contact of four-probe method, *Key Engineering Materials* 297 (2005) 610–615.
- [64] B. Bahtiri, B. Arash, S. Scheffler, M. Jux, R. Rolfes, A machine learning-based viscoelastic–viscoplastic model for epoxy nanocomposites with moisture content, *Computer Methods in Applied Mechanics and Engineering* 415 (2023) 116293.
- [65] X. Ji, S. Matsuo, N. R. Sottos, D. G. Cahill, Anisotropic thermal and electrical conductivities of individual polyacrylonitrile-based carbon fibers, *Carbon* 197 (2022) 1–9.

- [66] B. Bahtiri, B. Arash, S. Scheffler, M. Jux, R. Rolfes, A thermodynamically consistent physics-informed deep learning material model for short fiber/polymer nanocomposites, *Computer Methods in Applied Mechanics and Engineering* 427 (2024) 117038.
- [67] K. Levenberg, A method for the solution of certain non-linear problems in least squares, *Quarterly of applied mathematics* 2 (2) (1944) 164–168.